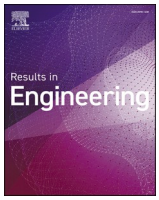
Results in Engineering 17 (2023) 100738



Contents lists available at ScienceDirect

Results in Engineering

journal homepage: www.sciencedirect.com/journal/results-in-engineering





Numerical and experimental investigation of surface-stabilized combustion in a gas-fired condensing boiler

Sandro Erne [a], Georg Scheger [b], Wolfgang Wiedemair [a,*]

[a] Institute for Computational Engineering, Eastern Switzerland University of Applied Sciences, Buchs, Switzerland
[b] Hoval AG, Vaduz, Liechtenstein

ARTICLE INFO

Keywords:
Laminar Combustion
NO_x
Porous Media
Surface-Stabilized Combustion

ABSTRACT

Gas-fired condensing boilers are widely used in domestic heating. However, emission of nitrogen oxides (NO_x) remains a concern due to their adverse environmental effects. Employing lean premixed surface-stabilized combustion, ultra-low NO_x generation is achievable.

We studied NO_x formation in realistic, axi-symmetric condensing boiler setups featuring lean combustion of methane stabilized by a porous cylindrical burner using a dedicated numerical model. To accurately represent the physical conditions, our model comprises most notably laminar combustion using a GRI-3.0 kinetic mechanism, a volumetric heat transfer coefficient for heat exchange inside the porous solid, conjugate heat transfer at the gas-solid interface and radiative heat exchange between burner surface and combustion chamber wall. A comprehensive assessment included validation of individual model aspects against literature data, a mesh study and validation with experimental measurements from a full-scale condensing boiler setup. Our findings suggest that the effective diffusion due to dispersive flow in porous media is critical for accurately capturing the reaction zone, thus preventing overprediction of flame temperature and NO concentration.

The dependencies of NO_x generation and heat release parameters on varying parametric and geometric configurations of the setup were assessed in a comprehensive numerical parameter study. We found that NO emission increases in a near-linear way with firing rate, while radiation efficiency decreases. At constant input power, NO emission rises with increasing equivalence ratio alongside radiation efficiency and peak flame temperature. By optimizing inflow uniformity, peak temperatures can be reduced by 9%, leading to significantly lower NO_x generation without affecting the heat flow rate.

1. Introduction

Nitrogen oxides (NO_x) are formed as undesirable by-products of the combustion of fossil fuels at high temperatures in e.g. by combustion engines and industrial processes. NO_x are among the dominant ozone-depleting substances as the production of ozone significantly depends on their concentration in the lower troposphere [6]. Numerous techniques have been extensively studied in the last decades to effectively reduce the formation of NO_x during combustion.

As high gas temperature in methane-air combustion increase the emission of NO_x substantially [33], ultra-lean combustion is one of the promising technologies due to its lower combustion temperature. Creating a flame with a high air-to-fuel equivalence ratio can contribute to decrease nitrogen containing toxins released from gas burners but also leads to combustion stability problems.

Energy generation from combustion of fossil fuels is likely to decrease in the coming decades [22,23] due to concerns about its impact on climate change. However, chemically similar, synthetic fuels (or e-fuels) which are created in a power-to-fuel process involving water, CO_2 and electricity, are expected to partially establish themselves as replacement [41]. Several different approaches to producing synthetic fuels exist, like adding acetylene to CH_4-rich combustion in porous media to increase the methane-syngas conversion efficiency, as studied in Ripoll et al. [34].

Using electricity produced from sustainable sources and CO_2 captured from the atmosphere, the synthesis and combustion cycle of e-fuels would qualify as CO_2-neutral. Despite significant energy conversion losses, e-fuels could be economically attractive since they avoid the necessity of engine technology transformation and are especially suitable for decarbonization of processes where direct electrification is not

* Corresponding author.
E-mail address: wolfgang.wiedemair@ost.ch (W. Wiedemair).

https://doi.org/10.1016/j.rineng.2022.100738
Received 28 July 2022; Received in revised form 15 October 2022; Accepted 28 October 2022
Available online 2 November 2022
2590-1230/© 2022 The Authors. Published by Elsevier B.V. This is an open access article under the CC BY-NC-ND license (http://creativecommons.org/licenses/by-nc-nd/4.0/).

(yet) a viable option such as air travel [49]. However, the combustion of e-fuels will still generate similar amounts of NO_x and other pollutants [25]. The further optimization of these combustion processes towards minimal pollutant production will therefore remain a focus and driver of future research. Hence, methods for reliably modeling fuel combustion processes with the aim of optimizing efficiency while reducing NO_x generation will likely remain highly relevant.

1.1. Combustion in porous media

Compared to conventional burners with a diffusive flame, combustion in porous media has different characteristics as heat is recirculated internally in the porous region to pre-heat the reactants and the temperature is lowered due to fluid-to-solid heat convection. Geometric characteristics, thermal and material properties have a significant impact on the flammability limits of fuel-air mixtures inside a porous media burner [38]. Hence, flame stabilizing effects and the influence of porous media on combustion have been subject to numerous numerical and experimental studies.

In Tierney et al. [39], ultra-lean methane-air combustion in porous solids was investigated using Computational Fluid Dynamics (CFD). An extensive numerical model that includes conjugate heat transfer as well as solid and gas radiation was implemented into a commercial CFD software.

Wang et al. [44] assessed the critical equivalence ratio of premixed methane-air combustion in porous inert media to better predict the thermal flame structure inside the porous burner. Barra et al. [3] reported that the efficiency of heat recirculation in porous burners increases with decreasing equivalence ratio and does not significantly depend on the length of the solid burner.

1.2. Surface-stabilized combustion

Improved combustion stability characteristics of lean natural gas-air mixtures can be maintained by utilizing surface-stabilized combustion (SSC) where the flame gets anchored on the burner surface due to heat exchange between the hot combustion zone and the porous solids. Domestic central heating appliances with a porous radiant burner for lean premixed methane-air combustion provide a broad stable modulation range and low combustion temperatures [14]. Thermal radiation is emitted by the hot surface of the metal fiber burner. Leonardi et al. [28] observed from experiments that the burner surface temperatures increase with the firing rate of the radiant gas burner as well as with increasing equivalence ratio.

Cylindrically shaped premixed perforated burners are widely used in condensing boiler technology for domestic central heating appliances. This burner technology combines high cost-efficiency with low emission levels and has been investigated in numerous studies.

In Schiro and Stoppato [36], the performance of a cylindrical premixed burner in combination with a condensing heat exchanger is studied experimentally. They found that porous steel burners with a metal fiber-type layer show an improved flame anchoring behavior for lean-mixture and high flow-rate combustion due to dominant radiative heat transfer.

Flame properties and flame stability were studied in Ref. [31] for a wide range of heating capacities and equivalence ratios (ϕ=0.4−1.2) by means of image processing methods. Optimal burner conditions yielding a stable blue flame were found in the range ϕ=0.7–0.73.

Colorado et al. [9] experimentally evaluated stability limits and emissions of SSC at the outflow of the porous media. In their experiments they observed a strong stabilizing effect of SSC for ultra-lean mixtures, yielding NO_x emissions below 10 ppm. Measurements of stability limits and pollutant concentrations of natural gas-fired boiler using a porous radiant burner are presented in Ref. [10]. For an equivalence ratio range of 0.7–0.8, NO_x concentrations in the range of 12–20 ppm were measured. Additionally, the important radiative heat transfer between gas zone and burner is addressed.

Evaluating surface-stabilized combustion in a porous inert media, Echeverri-Uribe and Amell [13] observed in their experiments a significant increase of NO_x pollutants as the specific power respectively the equivalence ratio was gradually increased.

Abdelaal et al. [2] analyzed the performance characteristics of porous radiant burners for various operating conditions. Experiments showed that an increasing firing rate leads to an increased burner surface temperature but to a lower radiation efficiency. Increasing the equivalence ratio from lean to rich revealed an increasing radiation efficiency as well.

The influence of radiative effects on the temperature field in the post-flame zone of a premixed and inert burner-stabilized flame is extensively investigated in Lammers et al. [26]. They found an increasing impact of radiative heat losses on the temperature field in the burning chamber for smaller burner geometries.

Focusing on the flame development near a perforated metal sheet under premix condensing boiler conditions, Hinrichs et al. [21] analyzed the NO_x formation in detail for different fuel mixtures using numerical and experimental methods.

Reviewing the available literature, the full numerical modeling of the convective and radiative heat exchange between the combustible flow and the porous burner as well as between the burner surface and the outer combustion chamber walls was identified as a research gap.

In the present work, a numerical method was developed that fully models the flame characteristics, considering the thermodynamic interaction between the gas flow and the surface-stabilized burner and the combustion chamber walls, focusing on the following aspects:

- development of a steady-state model for laminar combustion coupled with conjugate heat transfer including adjustable of material properties of the flame-stabilizing porous media
- implementation of the solver in an open-source CFD library
- verification of the developed numerical framework using experimental and numerical results of generic flow problems from literature
- validation of temperature and NO_x predictions in the combustion chamber with experimental data, obtained from a full-scale condensing boiler setup
- analysis of parametric simulation studies to better understand the influence of model parameters on the performance of the gas-fired condensing boiler, as well as the effect of thermophysical properties on the characteristics of SSC

2. Materials and methods

2.1. Experimental setup

All measurements and simulations were performed on the commercial condensing boiler *Hoval UltraGas®*, as shown in Fig. 1. The device mainly consists of a methane-air supply system including a centrifugal fan, a cylindrical combustion chamber, a heat exchange system and connections for exhaust gas and heating-circuit water. The lateral surface of the burner cylinder consists of two layers, an inner perforated metal sheet covered by a metal fiber mesh (FeCrAl alloy). This cylinder is centrally embedded in a larger cylindrical combustion chamber which itself is immersed in a heating-water tank. At the bottom of the combustion chamber a set of vertical heat exchanger tubes is attached, ensuring optimal transfers of the heat of the hot gas to the surrounding water of the heating circuit. Flue gas and condensate are discharged via a chimney or siphon.

An inflow with well-defined methane-air ratio is ensured by an arrangement exploiting the Venturi effect upstream of a centrifugal fan, which draws the fuel into the system. Gas and air are mixed passing the fan which is mounted at the inlet of a porous burner. The supply unit is optimized for continuous operation within a wide operating range and



Fig. 1. Detail view of the condensing boiler *Hoval UltraGas*® (3D rendering), including gas-air mixer, air blower, cylindrical premix burner and combustion chamber.

allows power modulation of the boiler by varying the fan rotation speed. Thereby the gas-air ratio changes in the range of a few percent. The boiler input power is monitored by a *Wolgroth*® rotary displacement gas meter during operation. The mixture ratio is subsequently calculated using the measured oxygen concentration. A high-precision gas meter is connected to the gas supply in order to accurately determine the inflow. Humidity, gas pressure and gas temperature in the gas line are taken into account to determine the output. The gas composition is provided by the gas supplier. The error tolerance for the calorific value is estimated to be 1%.

Fig. 2 shows a functional schematic of the condensing boiler. Multiple temperature sensors and a gas probe were inserted through specially made openings in the lid. Screwable sleeves were used and allowed to adjust the insertion depth continuously, even during operation. A total of four openings were fitted to the lid, two vertically facing down and two at an angle. An overview of all sample lines is given in Fig. 3. The measuring probes allowed measurements of temperature and combustion products both halfway between the burner surface and the combustion chamber wall and in the vicinity of the flame zone. The measuring probe, which can be moved at an angle to the burner axis, can monitor the combustion properties in the radial and axial directions over the entire metal fiber layer height. This measuring arrangement also allows non-uniform temperature distributions in the combustion chamber to be recorded.

2.1.1. *Temperature measurements*

The temperature measurements were carried out with a Al_2O_3-ceramic-coated thermocouple probe type S (inner diameter $D_{in} = 4$ mm and outer diameter $D_{out} = 10$ mm) from *Kull Instruments*®. As described above, the measuring positions could be adjusted via an adjustment mechanism during operation. For each measurement position along sample line A and B the process conditions were kept constant for 5 min and each measurement was repeated 3 times.

As the thermocouples are used in a high temperature environment (up to 1750 K) with cooled walls (inner temperature 400 K), heat

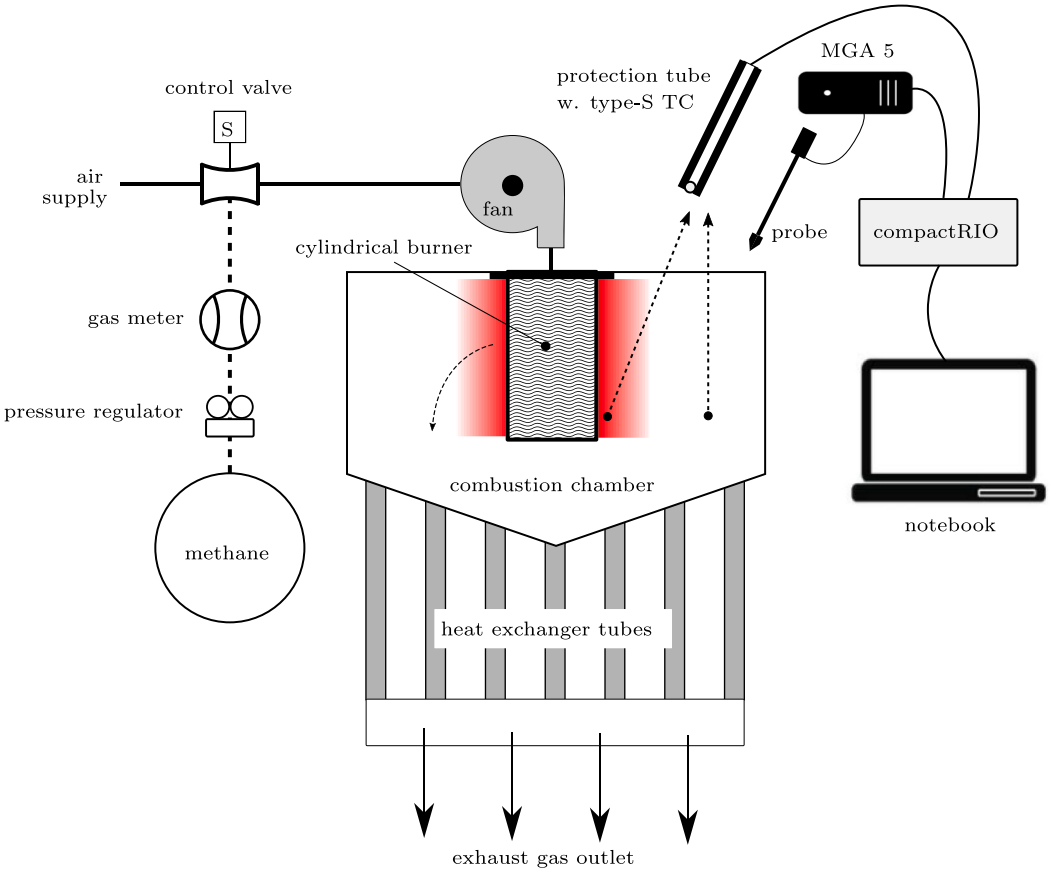


Fig. 2. Schematic of the experimental apparatus.

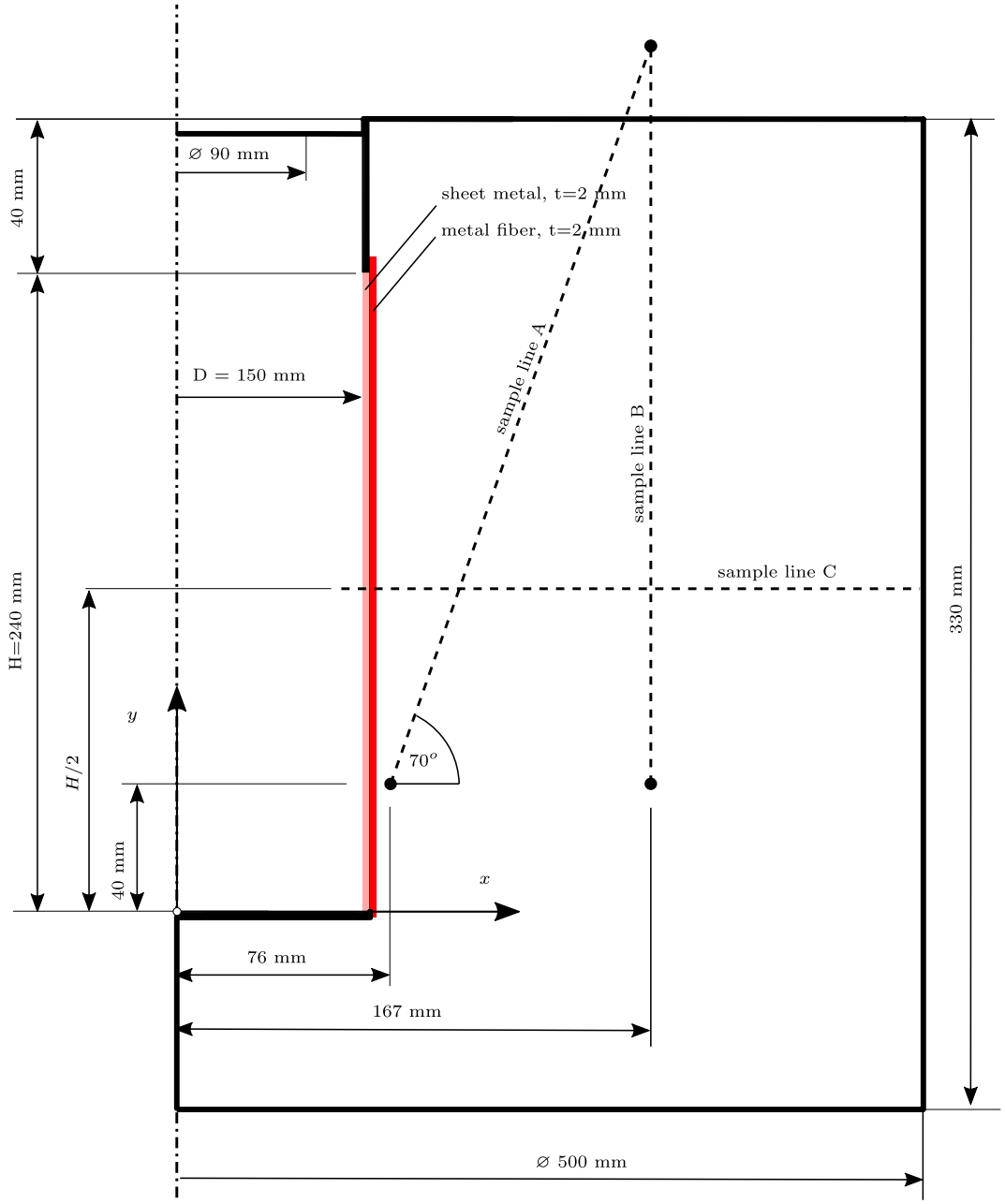


Fig. 3. Dimensions of the combustion chamber and position of sample lines A–C: inclined sample line for data validation (sample line A), vertical sample line for the temperature distribution along vertical axis of the cylindrical burner (sample line B), and radial sample line (only used in simulations) for radial profile of various quantities (sample line C).

exchange due to radiation occurs. Thus, radiation clearly affects the temperature measurement device and can cause significant temperature measurement uncertainties. This makes a radiation correction for the present measurement necessary, which is based on the consideration of convective heat transfer and radiative heat exchange with the environment of the thermal probe. Further details can be found in app. A.

2.1.2. Emission measurements

A high-precision gas meter is installed in the gas line in order to accurately determine the gas input rate. Ambient conditions as well as pressure and temperature in the gas line are taken into account to determine subsequently the correct volumetric gas flow. The gas consists mainly of methane, yet the exact composition, given by the gas provider, is considered to calculate the exact air-to-fuel ratio via the O_2 concentration which results in a correction of about 1% of its calorific value. Chemical balance equations are solved analytically considering N_2, O_2, Ar, CH_4, C_2H_6, C_3H_8, H_2. The gas concentrations were measured using a MGA 5 suction pyrometer (*MRU Gmbh*®), extracting 1 l/min.

2.2. Flow resistance

To determine the pressure loss across the perforated metal cylinder as well as the metal fiber layer, measurements of the pressure difference between the inside of the burner and the combustion chamber were carried out for different power settings, as listed in Table 1. The pressure difference Δp scales with the thermal input power P_{th} which itself is determined by the inflow velocity u_{in}. Based on these measured values, the characteristic Darcy coefficient $D = 2.56 \times 10^8$ m^{-2} and the Forchheimer

Table 1
Resistance characteristics of the porous media at different operating points of the condensing boiler.

P_{th} (kW)	u_{in} (m/s)	Δp (Pa)
150	3.80	170
90	2.28	80
45	1.14	30

coefficient $F = 2.7 \times 10^3$ m^{-1} were found, which are taken into account in the sink term of the momentum transport equation (see eq. (4)).

2.3. Numerical approach

In order to be able to analyze the flame development in the combustion chamber and the influence of the porous solids on the flame stability, numerical simulations were performed. In this work, the focus was put not only on the flame characteristics near the perforated combustion cylinder or the metal mesh attached to it, but on the flame propagation in the entire combustion chamber to gain a better understanding of the hot gas flow in the combustion chamber. The assumption of rotationally symmetric flow through the porous cylindrical burner and combustion chamber allows a reduction of the entire computational domain down to a 2D single wedge-type domain. Furthermore, the computational domain does not start directly at the inlet to the perforated metal cylinder, but already at the discharge of the fan, which also enables an evaluation of the inflow conditions to the porous combustion cylinder, which acts as a flow straightener too. To include the influence of the solid regions, namely sheet metal and metal fiber, on the flame characteristics the energy equation of these two solids is solved too. This allows convective heat transfer across the walls and also volumetric heat exchange between the fluid region and the solid regions. Verification tests of generic flow cases and validation simulations of the gas-fired condensing boiler were performed in steady state. After a carefully initialized starting solution, a stable flame response forms within a few iteration steps and thus has a clear advantage over the transient combustion simulations in terms of computation time. The gaseous flow in the combustion chamber is modeled of laminar type.

2.3.1. Computational domain

The computational domain of the analysis is subdivided into a single fluid region and two solid regions. The cell zones inside the porous solids on the fluid side, to which the volumetric heat exchange is applied, are marked red in Fig. 4, whereas the cell zones in the solid regions are marked blue.

All geometrical components of the fluid and solid computational domains were prepared using the software project SALOME® [7] that enables a full parametrization of all geometrical dimensions. The 2D-mesh export from SALOME® is transformed to a 2D axi-symmetric mesh. The mesh consists of mainly hexahedral and prism-type elements (see mesh statistics in Table 2).

The computational mesh is shown in Fig. 5. Fluid mesh zones which are interacting with solid mesh zones are refined to ensure 2–3 cell rows in radial direction, see Fig. 5-a.

Note that the boiler design includes a bundle of high-performance heat exchanger tubes which are connected downstream to the combustion chamber. The assumption of axi-symmetric flow conditions does not allow such an asymmetrical arrangement in the numerical model, however, the special layout of the tube exchanger has been approximated by multiple outlets at the bottom of the combustion chamber.

Table 2
Mesh statistics of the wedge-type computational domain.

type	number of cells
hexahedra	13,449
prisms	399
polyhedra	30

2.3.2. Governing equations

For modeling the steady laminar fluid flow with combustion and fluid-solid heat transfer in the 2D axi-symmetric geometry, governing equations are solved separately for fluid and solid zones. The governing equations were solved numerically using the finite volume method. The fluid-solid boundary interfaces are coupled by a thermal boundary condition, applied to physical walls. In the porous zones, the energy equations for fluid phase and solid phase are coupled through a volumetric heat transfer term.

As the computational domain has porous and free zones in both fluid and solid regions, additional source terms due to heat transfer may be activated by a dual switch, reading (Fig. 4)

$$\chi = \begin{cases} 1, \text{ porous zone (zones marked red / blue in Fig. 4)} \\ 0, \text{ free zone} \end{cases} \quad (1)$$

In the free fluid zones ($\chi = 0$), the porosity is set to $\varepsilon = 1$, whereas in the free solid zones $\varepsilon = 0$ is prescribed.

For the fluid phase, the governing equations are solved for mass, momentum, species and energy, similar to Ref. [26].

Mass conservation

The mass conservation of the steady-state compressible flow is given as follows:

$$\frac{\partial \varepsilon \rho u_j}{\partial x_j} = 0 \quad (2)$$

Momentum equation

The momentum of the fluid is solved by the following equation:

$$\frac{\partial}{\partial x_j}(\varepsilon \rho u_i u_j) = -\frac{\partial \varepsilon p^*}{\partial x_i} + \frac{\partial}{\partial x_j}\left[\varepsilon \mu \left(\frac{\partial u_i}{\partial x_j} + \frac{\partial u_j}{\partial x_i} - \frac{2}{3}\delta_{ij}\frac{\partial u_k}{\partial x_k}\right)\right] + \varepsilon S_i + \varepsilon B_i,\ i,j = 1,2,3 \quad (3)$$

where μ is the laminar viscosity. The Darcy-Forchheimer term is subdivided into a viscous loss part and an inertia loss part:

$$S_i = -\left(D\mu + F\frac{1}{2}\rho|u|\right)u_i \quad (4)$$

For simplicity, isotropic behavior of the porous resistance is assumed. Thus, D and F reduce to scalar values. The dynamic pressure in eq. (3) is defined as $p^* = p - \rho g_i x_i$ and the external body force due to buoyancy reads

$$B_i = -g_i x_i \frac{\partial \rho}{\partial x_i}. \quad (5)$$

Transport equation of species

The transport equation of the mass fraction Y_k of species k in a mixture with K species

$$\frac{\partial(\varepsilon \rho Y_k)}{\partial t} + \frac{\partial}{\partial x_j}\left(\varepsilon \rho u_j Y_k\right) = \frac{\partial}{\partial x_j}\left(\varepsilon k_f \frac{\partial Y_k}{\partial x_j}\right) + \varepsilon \dot{r}_k, \quad k = 1 \ldots K, \quad (6)$$

where $\dot{r}_k$ is change of the chemical rate.

Transport equation of energy in fluid region

For the fluid phase, the governing equation for enthalpy h_f is given as follows:

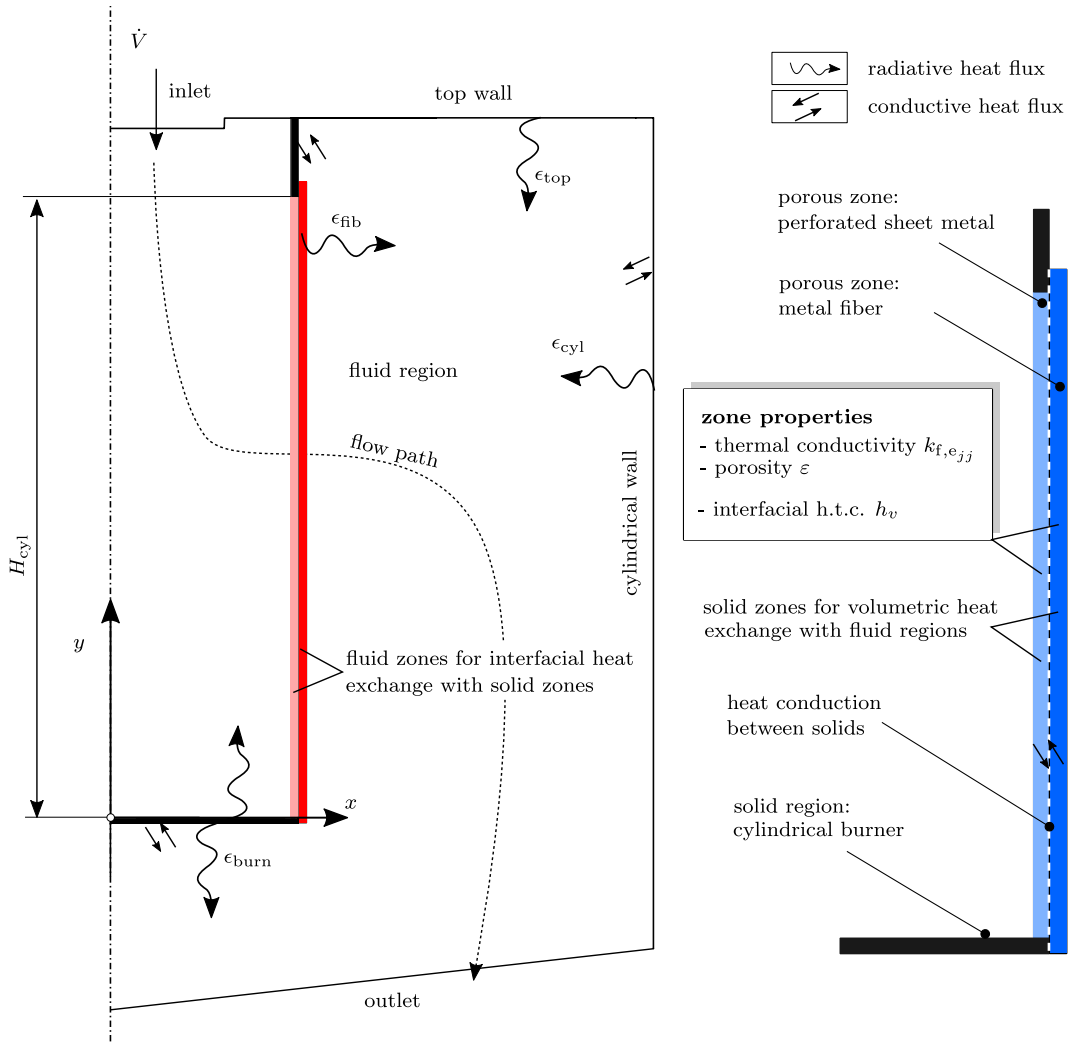


Fig. 4. Schematic of the axi-symmetrical wedge: the computational domain consists of the fluid region including the zones for volumetric heat transfer (red) which overlap with the sheet metal and metal fiber zones (blue) of the solid region (detailed in the right drawing). Important thermophysical parameters are given for each volumetric heat exchange zone pair. (For interpretation of the references to colour in this figure legend, the reader is referred to the Web version of this article.)

$$\varepsilon \frac{\partial}{\partial x_j}\left(\rho u_j h_f\right) = \varepsilon \frac{\partial}{\partial x_j}\left(\frac{k_{f_{jj}}}{c_{p,f}} \frac{\partial h_f}{\partial x_j}\right) + \chi h_v \left(T_s - T_f\right) + S_r + \varepsilon \sum_{i=1}^{N_s} \dot{r}_{k,i} h_i \tag{7}$$

where $k_{f_{jj}} = \chi k_{f,e_{jj}} + (1-\chi)\delta_{jj} k_f$ denotes the tensorial thermal conductivity, which equals to the effective thermal conductivity $k_{f,e_{jj}}$ in the porous regions, as outlined in app. C. S_r is the source term due to radiation and N_s is the number of species. The volumetric heat transfer between fluid and solid structures is parametrized separately for each solid region by means of the volumetric heat transfer coefficient. As in Zeng et al. [50], the volumetric heat exchange between fluid zone and the perforated zone of the metal cylinder is characterized by the volumetric heat transfer coefficient $h_v = 6\varepsilon \mathrm{Nu}_v k_g / d_s^2$, assuming local thermal non-equilibrium. Further, the Nusselt number is defined as $\mathrm{Nu}_v = 2 + 1.1 \mathrm{Pr}^{1/3} \mathrm{Re}^{3/5}$. The characteristic length is denoted by d_s. For the metal fiber, a volumetric heat transfer coefficient $h_v = \tanh(m d_p/2)\, m k_s d_{fib}/d_p$ was prescribed, where the fiber diameter is $d_{fib} = 1$ mm and the cell size is assumed with $d_p = 2$ mm. Refer to Wang et al. [45] for further details. The diffusivity term in eq. (7) is based on a simplified molecular transport model which assumes a unity Lewis number and does not take into account differential diffusion between the species or effects due to thermophoresis. This can result in an inaccurate prediction of relevant physical processes in the combustion, especially at higher equivalence ratios.

Radiation in fluid region

In high-temperature combustion chambers, thermal radiation is transmitted to the solid directly from the flame. For all simulations including radiative heat transfer, the simple P_1 radiation model is applied. The transport equation of the total incident radiation G reads

$$\frac{\partial}{\partial x_j}\left(\Gamma \frac{\partial G}{\partial x_j}\right) = 3\kappa^2 (G - 4\sigma T_f^4) \tag{8}$$

where κ is the absorption coefficient, Γ denotes the diffusivity and T_f is the absolute fluid temperature. Scatter radiation is neglected. For the incident radiation field G the Marshak boundary condition is applied

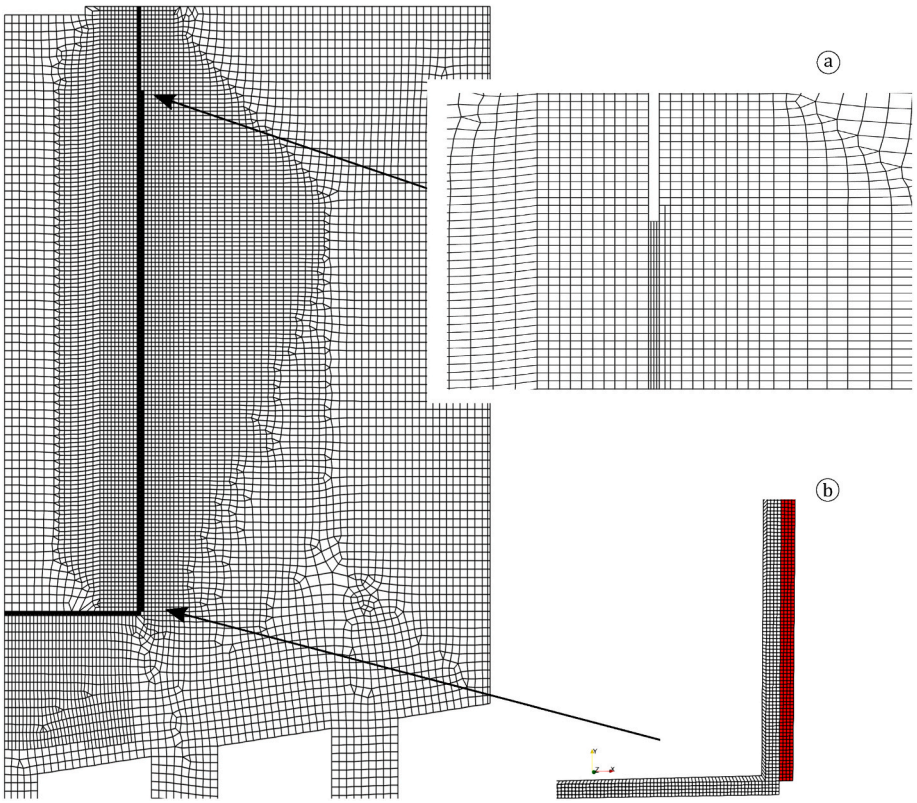


Fig. 5. Mesh plots of the computational domain: fluid region with detail plot (a) and solids cylindrical burner and metal fiber (marked red) (b). (For interpretation of the references to colour in this figure legend, the reader is referred to the Web version of this article.)

which accounts for the radiation emitted/absorbed by the domain boundaries. To account for optically thin gases in the computational domain, the gray-mean-absorption-emission model is used which assumes a spectrally constant absorption coefficient. The radiation absorption coefficient α of radiating flue gases, mainly CO_2 and H_2O, is calculated for each computational cell of the fluid zone.

Compared to more complex modeling strategies of gaseous radiation, the model presented herein is one of the simplest. Since an axisymmetric computational domain was used in this work, a radiation model based on the discrete ordinates method is not applicable. For the used P_1 model, however, a reasonable accuracy for methane-air combustion regimes and a high computational efficiency has been found in Garten et al. [18].

Transport equation of energy in solid regions

For the solid phases, the governing equation for enthalpy h_s is solved, given by

$$\frac{\partial}{\partial x_j}\left((1-\varepsilon)k_s\frac{\partial h_s}{\partial x_j}\right)+\chi h_v\left(T_f-T_s\right)=0. \tag{9}$$

Radiation in the porous solid zone is neglected.

2.3.3. Boundary conditions and initial state

A detailed overview of all used boundary values as well as initial values of both fluid and solid region is given in Table 3.

Fluid region

- a premixed methane-air mixture enters the domain inlet at $T_{in} = 293$ K
- the top wall of the combustion chamber is defined as adiabatic wall
- for the heat transfer boundary condition at the outer surface of the cylindrical wall of the combustion chamber, a constant water temperature of 300 K and a total heat transfer coefficient $h = 100$ W $m^{-2}K^{-1}$ is prescribed
- coupled heat transfer between fluid and solid region on all remaining wall-type boundaries. At the wall-type fluid-solid interfaces, a local thermal equilibrium is assumed, as described in [8].
- no-slip boundary conditions are prescribed for the physical walls in the fluid region
- atmospheric pressure is defined at the domain outlet
- for solving the thermal radiation transfer, the Marshak boundary condition is applied at the wall boundaries
- radiative heat exchange between the metal fiber outlet and the downstream combustion chamber wall is taken into account. As the solid boundary of the cylindrical burner does not define a physical boundary of the fluid zone, a Marshak boundary condition is not applicable. However, a simple radiative coupling method based on analytical aspects is implemented instead. The net radiative flux between the outer surface of the fiber in the solid region and the cylindrical wall of the combustion chamber in the fluid region is defined by a simple surface-to-surface approach, reading

Table 3
Summary of material properties and boundary values for operating point $P_{th} = 90$ kW at $\phi = 0.74$, including references for the most important material properties.

patch/zone	expression	value	unit	description
fluid region				
Inlet				
	Y CH_4	0.0420	kg kg^{-1}	mass fraction methane
	Y O_2	0.2231	kg kg^{-1}	mass fraction oxygen
	Y N_2	0.7348	kg kg^{-1}	mass fraction nitrogen
	T_{in}	293	K	inlet temperature
	$\dot{V}$	0.0023	m^3s^{-1}	volumetric inflow
top wall (steel)				
	ϵ_{top}	0.7	–	emissivity, oxidized rolled alloy, Maznoy et al. [29]
bottom wall (steel)				
	ϵ_{bot}	0.7	–	emissivity, oxidized rolled alloy, Maznoy et al. [29]
cylindrical wall (steel)	ϵ_{cyl}	0.7	–	emissivity, oxidized rolled alloy, Maznoy et al. [29]
	h_{cyl}	100	W $m^{-2}K^{-1}$	external heat transfer coefficient
	T_{cyl}	300	K	average water temperature
	k_{cyl}	25	W $m^{-1}K^{-1}$	thermal conductivity burner (stainless steel)
fluid zone metal fiber				
	$k_{f,stag}$	(16.4469 16.4469 16.4469)	W $m^{-1}K^{-1}$	thermal conductivity tensor (rr, $\phi\phi$, zz)
	$k_{f,disp}$	(0.4458 0.0223 0.0223)	W $m^{-1}K^{-1}$	thermal dispersion tensor (rr, $\phi\phi$, zz)
fluid zone perforated sheet metal				
	$k_{f,stag}$	(0.0798 31.346 31.346)	W $m^{-1}K^{-1}$	thermal conductivity tensor (rr, $\phi\phi$, zz)
	$k_{f,disp}$	(1.9104 0.0955 0.0955)	W $m^{-1}K^{-1}$	thermal dispersion tensor (rr, $\phi\phi$, zz)
solid regions				
cylindrical burner				
	k_{burn}	25	W $m^{-1}K^{-1}$	thermal conductivity (stainless steel)
	c_p	460	J $kg^{-1}K^{-1}$	specific heat capacity
	ϵ_{burn}	0.55	–	porosity, measured
	ρ	7700	kg m^{-3}	density
	t	2	mm	wall thickness
metal fiber				
	k_{fib}	16	W $m^{-1}K^{-1}$	thermal conductivity
	ϵ_{fib}	0.65	–	emissivity, Golombok et al. [19]
	c_p	700	J $kg^{-1}K^{-1}$	specific heat capacity at 1400 K, Field et al. [15]
	ε_{fib}	0.2659	–	porosity, measured
	ρ	550	kg m^{-3}	density
	t	2	mm	wall thickness

$$q_{r,fib-cyl} = \frac{\sigma}{\frac{1-\epsilon_{fib}}{A_{fib}\epsilon_{fib}} + \frac{1}{A_{fib}F_{fib-cyl}} + \frac{1-\epsilon_{cyl}}{A_{cyl}\epsilon_{cyl}}} \left(T_{fib}^4 - T_{cyl,av}^4\right) \quad (10)$$

where $F_{fib\text{-}cyl}$ denotes the view factor of two concentric cylinders of finite length [30] (p.771), T_{fib} is the local temperature at the fiber outlet patch and $T_{cyl,av}$ is the area averaged temperature of the cylindrical wall of the combustion chamber. The emissivity of the metal fiber layer and the combustion chamber wall is ϵ_{fib} and ϵ_{cyl} respectively. In this simplified model, only the cylindrical part of the combustion chamber walls (A_{cyl}) is taken into account for radiative heat exchange with the outer metal fiber surface A_{fib}.

- after reaching steady-state conditions of the premixed flow, in the porous section the fluid part is set to 1700 K and the metal fiber region is set to 1200 K to ignite the flame

Solid regions

- adiabatic behavior is prescribed to the cylindrical face at the top of the cylindrical burner
- conjugate heat transfer between solid and fluid region on all remaining solid walls
- conductive heat transfer between the solid regions cylindrical burner and metal fiber

2.4. Numerical details and solution method

All simulations were carried out using OpenFOAM® [46] (OF) version 5.x. In order to completely capture all thermophysical processes in surface-stabilized combustion, the existing standard application `chtMultiRegionSimpleFoam` provided in OF was adapted accordingly.

A schematic of the workflow including the solver structure is given in Fig. 6. The geometry is prepared in SALOME® where an arbitrary cross-sectional area is defined for each region. A hexahedral mesher is applied on the extruded cross-sections to generate structured 2D meshes which are then flattened in OF.

After initializing the temperature fields, the transport equations are first solved for the fluid region. First, the momentum equation including source terms due to buoyancy and porous resistances is solved. The mass conservation of all species is calculated after updating the diffusion properties for the porous regions. The energy equation of the fluid domain is solved by taking into account the conjugate heat fluxes, the volumetric heat exchanges between the solid and fluid, as well as the radiative heat transfer according to the heat flux scheme shown in Fig. 7. Last the velocity-pressure coupling is solved by applying the SIMPLE-algorithm. The energy balance in the solid regions is computed from the conjugate heat fluxes across fluid/solid and solid/solid interfaces, as schematically shown in Fig. 7. Finally, the performance indicators listed in sec. 2.4.1 are calculated after a converged flow solution is reached.

For the fluid region, a flux-blending discretization (switches between 1st-order differencing scheme and 2nd-order differencing scheme) was

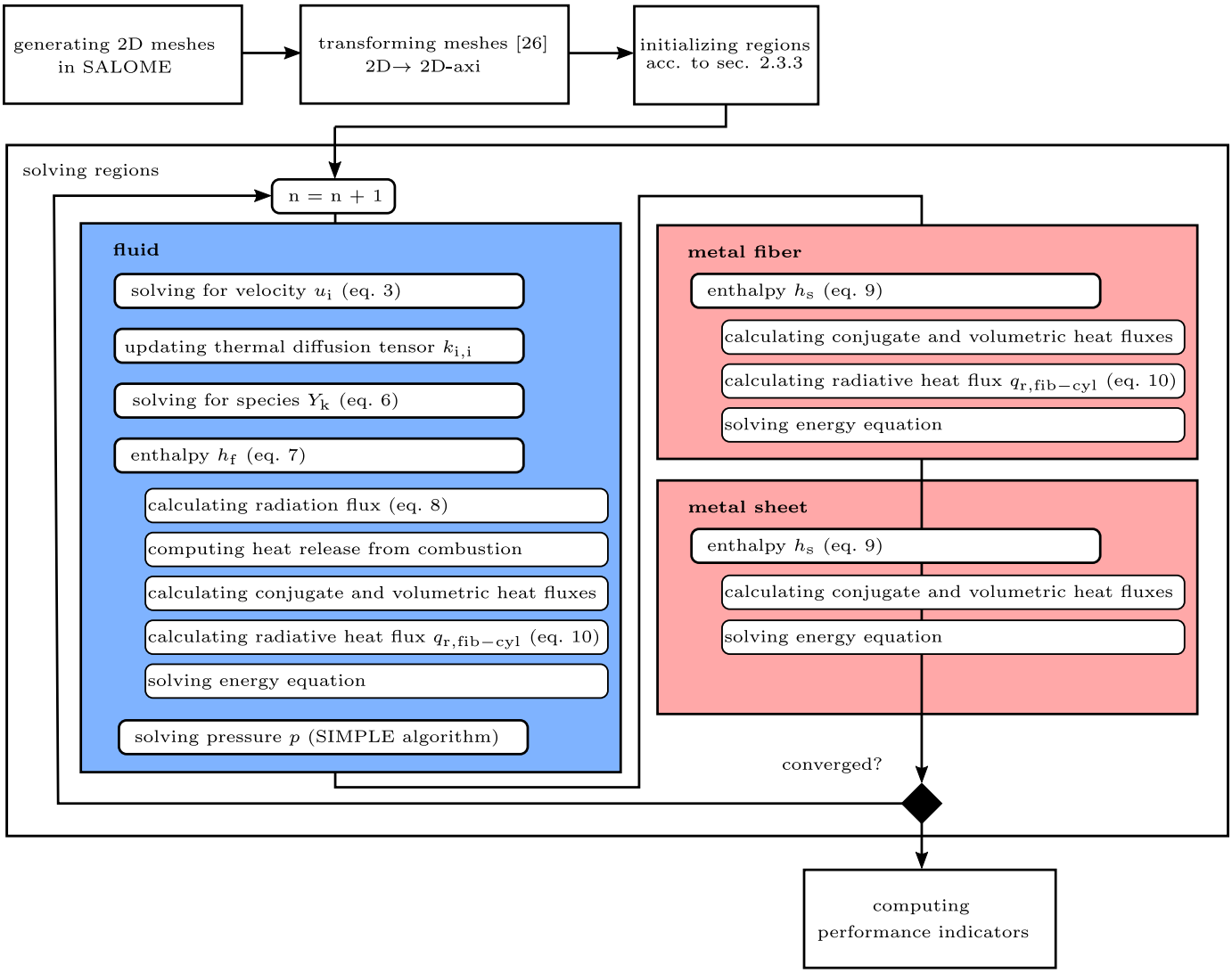


Fig. 6. Diagrammatic description of the flow problem, including the solving procedure for each region.

used for all convection terms which yields more numerical robustness. For the diffusion terms of the transport equations, a corrected linear interpolation scheme was applied.

The chemical kinetics are solved by the `EulerSI` solver, using a relative tolerance of 1×10^{-1} and an absolute tolerance of 1×10^{-7}. Volumetric energy transfer between the physical regions is introduced via the flexible framework `fvOptions` in OF. The existing class `variableHeatTransfer` was adapted.

For all combustion test cases conducted in this work, the detailed kinetic mechanism GRI 3.0 (number of species = 53 and reactions = 325) was used. It includes NO formation and reburn chemistry (see Frenklach et al. [16] for more details). A comparison of the well-known kinetic mechanisms GRI 3.0 [16], Konnov [24], San Diego [1] has shown that for both fuel-rich and fuel-lean CH_4-flames GRI 3.0 revealed most reasonable agreement of NO formation between simulation and experiments.

2.4.1. Performance parameters

Progress variable c

The flame structure is assessed by means of the progress variable c of the premixture, as proposed in Poinsot and Veynante [32]:

$$c = \frac{Y_{\text{fuel}} - Y^u_{\text{fuel}}}{Y^b_{\text{fuel}} - Y^u_{\text{fuel}}} \tag{11}$$

where Y^u_{fuel} is the flow-weighted mean mass fraction of the fuel composition at the inlet and Y^b_{fuel} denotes the mass fraction at the outlet.

Radiation efficiency η_{rad}

The radiation performance of the cylindrical burner is evaluated by the radiation efficiency, based on the net radiative heat flux between metal fiber and the cylindrical combustion chamber wall:

$$\eta_{\text{rad}} = \frac{q_{\text{r,fib-cyl}}}{F_{\text{R}}} \cdot 100\% \tag{12}$$

Herein, the firing rate $F_R = P_{\text{th}}/A_{\text{fib}}$ is applied on the surface area of the metal fiber outlet.

Energy conversion efficiency ζ

The ratio between the total rate of heat flow across the cylindrical part of the combustion chamber and the thermal input may reads

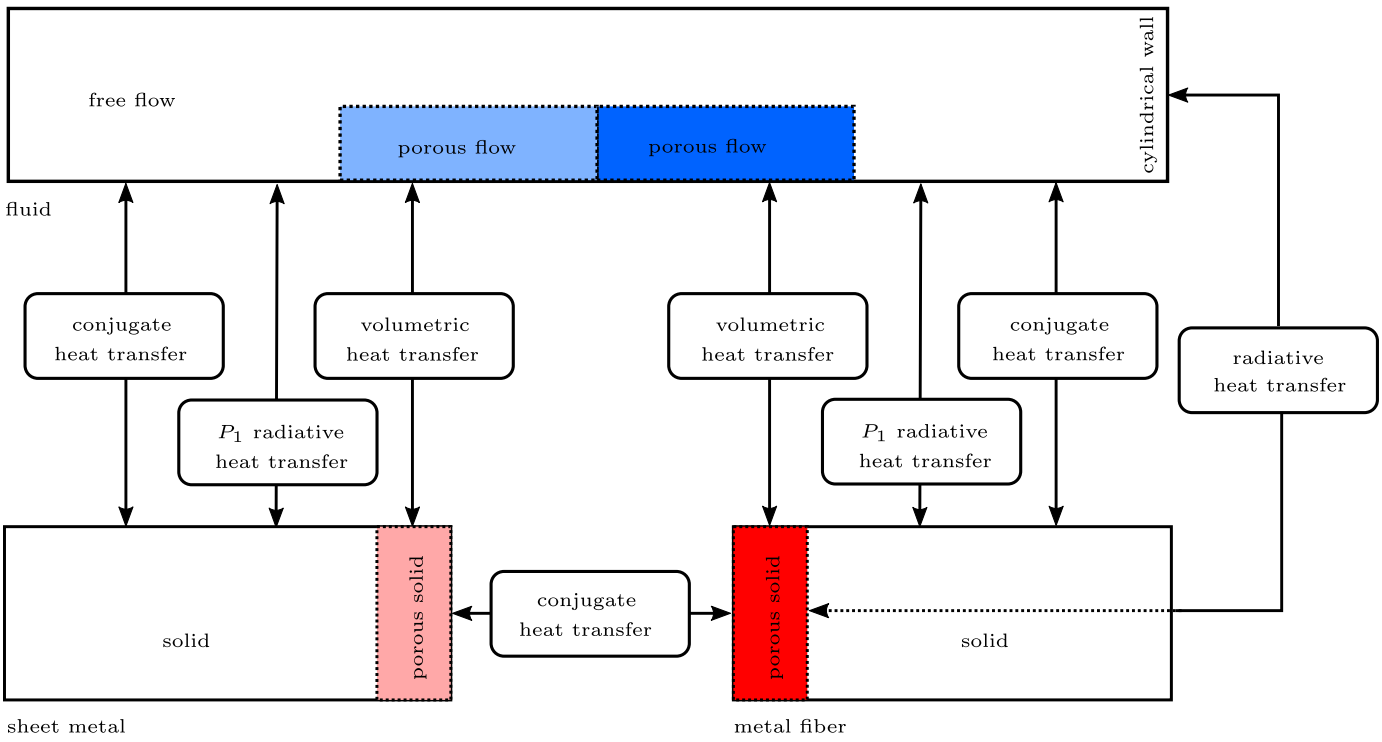


Fig. 7. Schematic of volumetric/conjugate heat transfers between the fluid and the solid regions (sheet metal/metal fiber).

Table 4
Simulation data of the grid study: volume-weighted temperature, characteristic grid width near the combustion area and computation time for three refinement levels.

refinement level j	temperature $\overline{T}_{\mathrm{f},j}$ (K)	grid width h_j (mm)	clock-time (s)
1 (fine)	978.3	0.575	4408
2 (medium)	971.8	1.15	2739
3 (coarse)	954.3	2.3	1067

$$\zeta = \frac{Q_{\mathrm{cyl}}}{P_{\mathrm{th}}} \cdot 100\% \tag{13}$$

where Q_{cyl} includes the convective heat flux and radiative heat fluxes:

$$Q_{\mathrm{cyl}} = A_{\mathrm{cyl}}(q_{\mathrm{conv}} + q_{\mathrm{r,fib-cyl}} + q_{P_1}) \tag{14}$$

In eq. (14), A_{cyl} denotes the surface area of the cylindrical part of the combustion chamber and $q_{\mathrm{P_1}}$ denotes the incident radiative wall heat flux from the $\mathrm{P_1}$ model.

3. Results and discussion

Relevant physical sub models of the full numerical model such as radiation, conjugate heat transfer, characteristics of the used kinetic mechanism and combustion were verified by comparison to specific flow problems from literature, as detailed in app. B.

3.1. Grid independence study

Simulations for $P_{\mathrm{th}} = 90$ kW were conducted on a coarse, medium and fine mesh to evaluate the numerical accuracy, as proposed in Roache [35]. The volume-weighted fluid temperature $\overline{T}_{\mathrm{f}}$ of the entire fluid volume was used for error estimation. The mesh region near the porous zones was gradually refined in OF. The order of accuracy p is calculated as follows:

$$p = \frac{\ln\left(\frac{\overline{T}_{\mathrm{f},3} - \overline{T}_{\mathrm{f},2}}{\overline{T}_{\mathrm{f},2} - \overline{T}_{\mathrm{f},1}}\right)}{\ln(r)} \tag{15}$$

Using a refinement ratio $r = 2$ and the temperature values $\overline{T}_j$ from Table 4 eq. (15) yields $p = 1.4$.

The relative error between two refinement levels is defined as $\varepsilon_{i,j} = (\overline{T}_{\mathrm{f},i} - \overline{T}_{\mathrm{f},j})/\overline{T}_{\mathrm{f},i}$. In Fig. 8-left the radial profile of the temperature is shown in for different mesh refinement levels j along sample line C. The inspected temperature close to the metal fiber shows a monotonic convergence behavior with a reasonable order of convergence, as illustrated by $\varepsilon_{0,j}$ over h in Fig. 8-right.

Note that the relative error values in Fig. 8-right were calculated using $\overline{T}_{\mathrm{f},0} = \overline{T}_{\mathrm{f},1} + (\overline{T}_{\mathrm{f},1} - \overline{T}_{\mathrm{f},2})/(r^p - 1) = 982.3$ K from a Richardson extrapolation which is an estimate of the temperature at zero grid spacing $h = 0$.

3.2. Model accuracy

The present numerical model consists of several physical sub-models. In order to assess the impact of each of those model components on the flame response, simulations of the condensing boiler at a fixed operating point ($P_{\mathrm{th}} = 90$ kW) were performed applying different model configurations:

- Model A: full model including all porous parameters
- Model B: Model A without taking into account the effective diffusion due to dispersive flow in porous media
- Model C: Model B without heat exchange between the solid porous phase and the fluid phase
- Model D: Model C without modeling Darcian resistance due to the porous media flow

Fig. 9 displays the radial profiles of the gas temperature and NO formation for the models A-D. For Model A, the combustion zone is situated inside the inert porous solid (submerged combustion). Model B

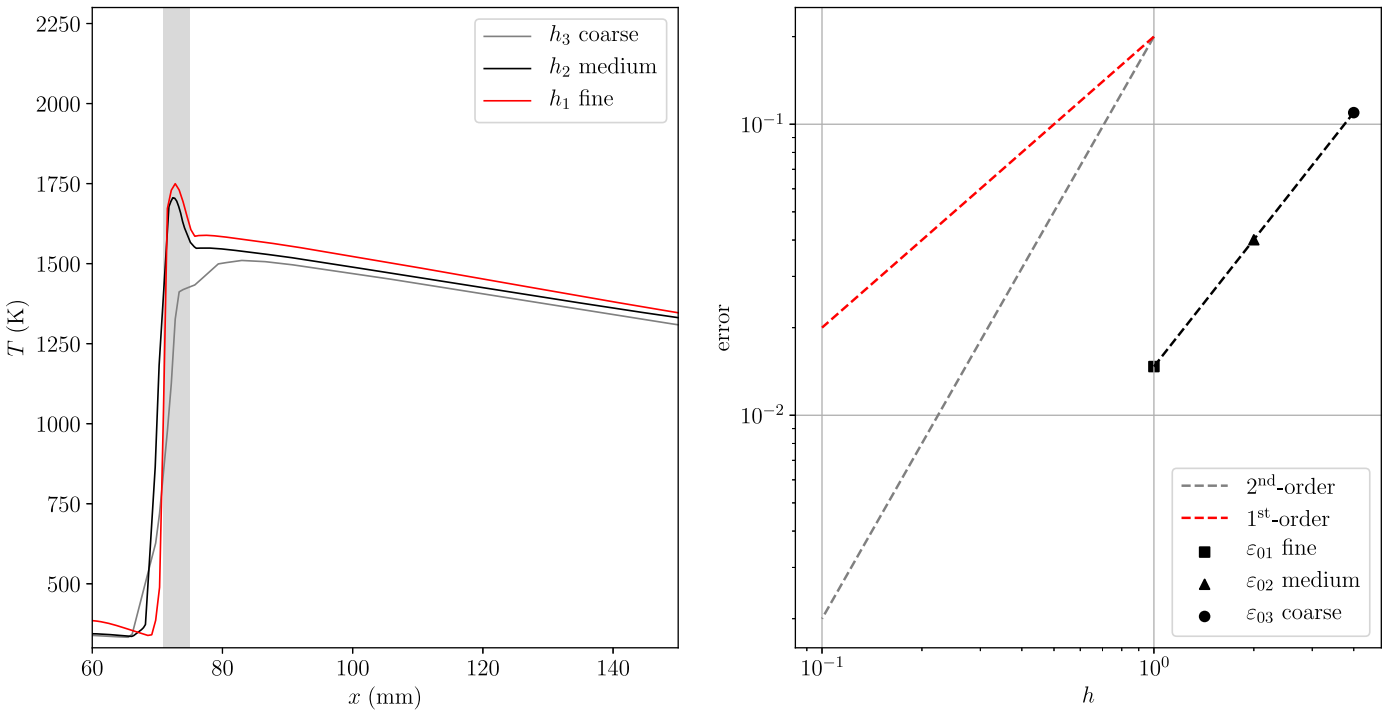


Fig. 8. Temperature distribution along sample line C for different mesh refinement levels. The coarse mesh shows a flame front outside the porous domain (gray), whereas medium and fine mesh capture the flame front inside that region (left). Convergence of the volume-weighted temperature over normalized grid spacing h (right).

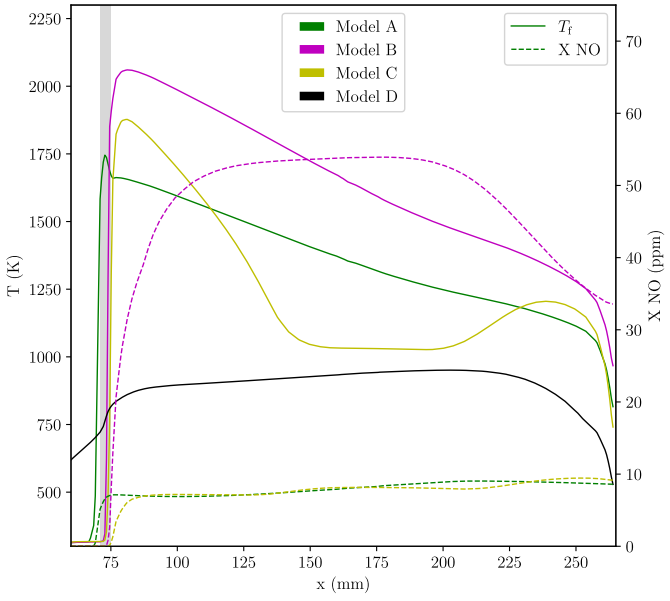


Fig. 9. Radial distribution of temperature T_f and NO concentration for the model configurations A-D at $H/2$. Porous zone marked in gray.

shows a flame front anchored outside the porous fiber zone which results in an overprediction of the maximum flame temperature as well as excessive NO concentration. Partial flame lift-off is observed for Model C and complete loss of stabilization occurs in Model D.

As shown in Fig. 10 by the progress variable c (see eq. (11)), model configuration A yields a stable combustion zone inside the metal fiber over the entire burner height. Slight differences in the radial position of the reaction zone are observed, which can be primarily attributed to the different inflow velocities over the burner height. Model B shows a uniformly burning flame, however, a reaction front forming upstream of the porous zone can be observed at the very bottom of the cylindrical burner. On the other hand, the flame stabilizes outside the porous zone in the upper region of the cylindrical burner, resulting in a lack of heat transfer from the combustion gas to the radiating solid fiber mesh. A flame attached to the porous medium can be seen for model C, which shows partial flame lift-off. As expected, no stable flame is observed using model D. Instead, a flame front appears in the middle of the combustion chamber. To achieve a stable flame response over the entire metal fiber layer, all the analyzed fundamental physical processes have to be taken into account in the numerical model.

3.3. Model validation

Using the experimental setup described in sec. 2.1, various temperature and gas species concentration measurements were taken in the combustion chamber of a full-scale condensing boiler. These serve as experimental reference for a comprehensive validation of the full numerical model of the gas-fired condensing boiler. In Fig. 11-a to Fig. 11-d, the flame structure from simulation results is compared to the measurement data along sample line A. The axial temperature distribution in the combustion chamber is validated by measurements along sample line B, as shown in Fig. 11-e. The chart shows the flame temperatures and profiles of major dry species for a methane flame at $\phi = 0.74$ at several input power levels, ranging from $P_{th} = 30$–120 kW.

The radial temperature distribution of the flame is shown in Fig. 11-a. At the 90 kW operating point, a temperature peak of 1750 K is observed in the porous region, which is approx. 100 K below the adiabatic temperature of a methane-air flame at $\phi = 0.74$. Due to radiative cooling at the outer surface of the metal fiber region, a sudden temperature drop of 100 K is observed in the simulated flame. Both the numerical results and the measured temperature show a sharp drop of approximately 300 K between 120 mm and 160 mm. The reason for this is that the sampling points are located in a region where the hot gas flow downstream of the flame zone forms a cooled recirculation zone, developing under the top lid of the combustion chamber, see Fig. 16. An

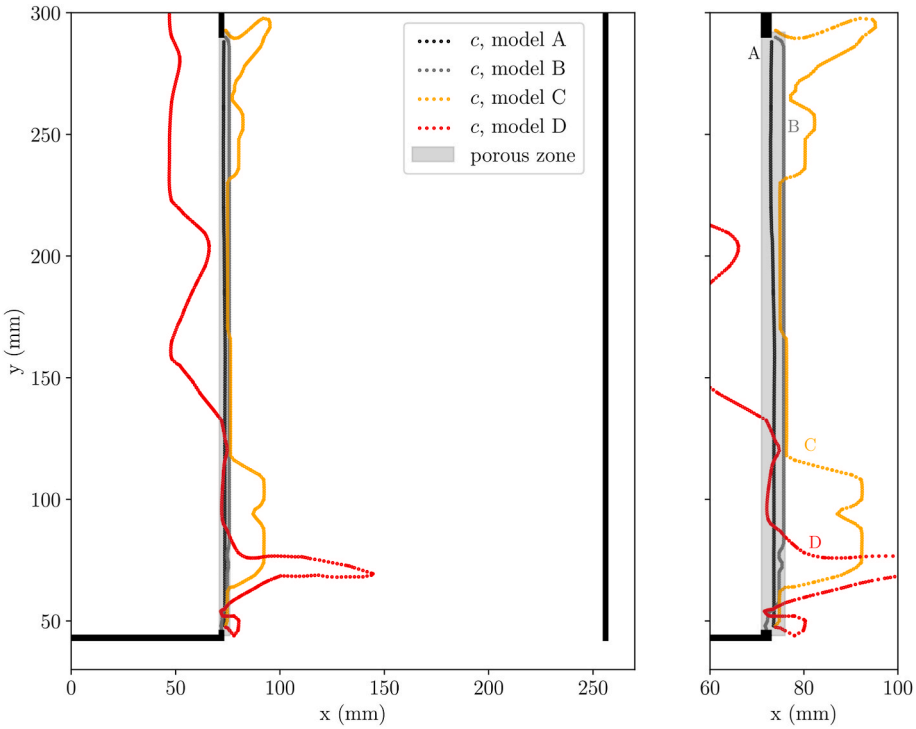


Fig. 10. Reaction zone inside the combustion chamber outlined using the 50%-iso line of the progress variable c for different model configurations: A (full model), B, C and D. Zoomed view on porous zone (right). Porous zone marked gray.

inspection of the flow field shows, that the radial flow of hot flue gas coming from the cylindrical burner impinges the outer combustion chamber wall and gets divided into two branches. The main part flows directly towards the downstream heat exchanger section, while the remaining part flows upwards and recirculates back to the flame, after being cooled down along the combustion chamber wall. Compared to experimental data, the temperature in this upper recirculation zone of the combustion chamber (see Fig. 11-a at $x = 150$ mm) is considerably underestimated by 200 K, possibly due to enhanced wall heat transfer in the upper part of the cylindrical combustion chamber wall.

Fig. 11-d shows that the measured NO concentrations for 90 kW tend to be underestimated by the simulation by 5 ppm on average. In addition, the simulated curve shows that the production of NO fluctuates strongly along the height of the burner cylinder, caused by a slightly non-uniform vertical temperature distribution within the combustion zone. Varying NO concentrations at different axial positions in the post flame region of a cylindrical burner were also observed from measurements in Ref. [21].

A slight increase of the NO-concentration can be seen for an increasing input power. The concentrations for O_2 (4.85%) and CO_2 (7.3%) of the dry exhaust gas along the evaluation line correlate well with the measured values across the combustion chamber. In the center of the combustion chamber the simulated temperature agrees with the measurement but significantly decreases in the upper chamber region, starting at $z = 250$ mm (see Fig. 11-e).

3.4. Parameter studies

In this section, the influence of important process parameters on the performance indicators of the gas-fired condensing boiler is assessed.

3.4.1. Variation of input power

The temperature distribution in the combustion chamber is shown for various power inputs in Fig. 12. With increasing velocity at the domain inlet, a backflow region of unburnt gas is forming between the domain inlet and the inlet of the perforated sheet metal in the upper burner cylinder region. This is mainly caused by the backward facing step between domain inlet and the inlet of the porous section, where the flow gets partially divided due to the Darcian flow resistance. Further, the upper flow branch is getting heated up due to convective heat transfer at the hot porous inlet and recirculates back to the cold inflow, see Fig. 12-c and 12-d. From Fig. 12-d, a starting lift-off of the flame due to an increased flow velocity can be observed at $H/2$.

At low input power ($P_{th} = 30$ kW), the simulation yields a maximum flame temperature as low as 1500 K, resulting in a very low averaged NO emission at the domain outlet, as can be seen in Fig. 13-top. Maximum gas temperature of 1720 K is reached at a firing rate of $F_R = 1100$ kW/m^2 (see eq. (12)). Compared to the maximum gas temperature $T_{f,max}$, the average surface temperature of the metal layer T_{fib} shows a similar trend over the output power range of the boiler. The simulation results show that the surface of the metal fiber layer can reach temperatures ranging from 1170 K at $F_R = 250$ kW/m^2 to 1480 K at $F_R = 1100$ kW/m^2. The NO emission increases in a near-linear way with input power. The variability band shows that even at constant temperature field, the steady-state solver calculates a fluctuation of NO concentration at the outlet, which increases as the maximum temperature in the combustion chamber increases. The reason for this may be that the flame structure in the region of the porous medium no longer assumes a steady state due to an increasing non-uniformity of the inflow.

In Fig. 13-bottom, the radiation efficiency η_{rad} (see eq. (12)) and energy conversion efficiency ζ (see eq. (13)) as a function of the firing rate F_R are shown. The diagram shows that both parameters decrease as F_R increases. Similar characteristics were observed in experiments from Ref. [28], who measured $\eta_{rad} = 22\%$ for $F_R = 350$ kW/m^2, however, at $\phi = 0.9$. Fursenko and Maznoy [17] and Abdelaal et al. [2] also detected a decreasing radiation efficiency with increasing firing rate in experiments on radiation characteristics of a porous burner. This dropping efficiency with increasing firing rate can be explained by the fact that due to the higher thermal load on the metal fiber, the flame increasingly moves outside the porous medium and can transfer less heat to the metal fiber, even though the interfacial heat transfer coefficient increases.

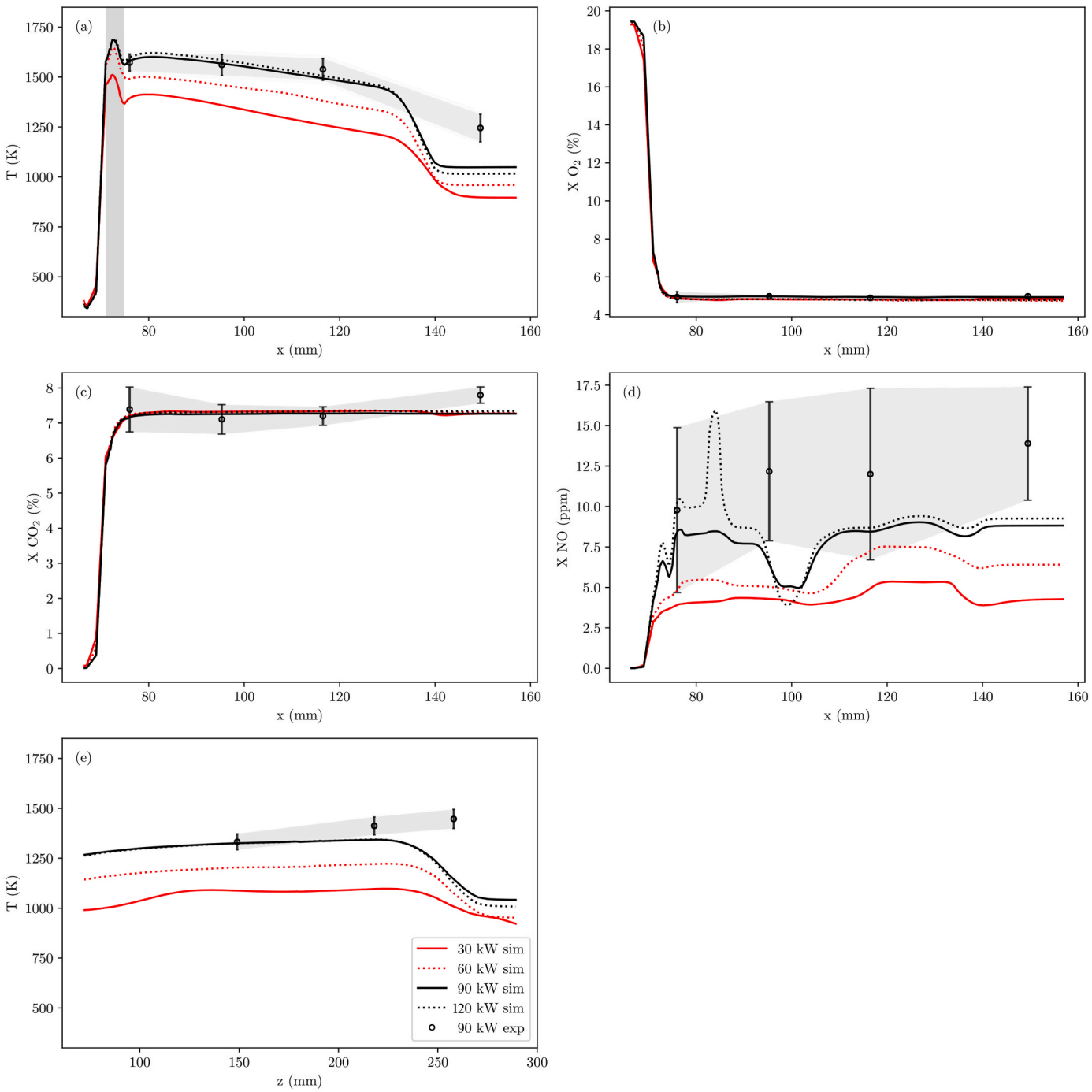


Fig. 11. Comparison of simulation results with experimental data for different P_{th}. Along sample line A: gas temperature (a), O_2 concentration (b), CO_2 concentration (c), NO concentration, featuring substantial fluctuations along the cylindrical axis (d). Gas temperature along sample line B (e).

3.4.2. *Variation of equivalence ratio*

The response of the flame to a varying equivalence ratio is determined by varying ϕ from 0.64 to 0.95 at a constant thermal input power $P_{th} = 90$ kW. Fig. 14 shows the variation of the maximum gas temperature T_{max} along sample line C and variation of the mean NO concentration at the domain outlet as a function of the equivalence ratio. As expected, the NO formation considerably increases as ϕ gets closer to one. Near stoichiometric conditions at $\phi = 0.95$, the maximum gas temperature of 1880 K is still significantly below the adiabatic flame temperature, peaking around 2200 K. Similar to the temperature curve, η_{rad} of the cylindrical burner increases from 13% to 19%, as more heat is transferred from the gaseous active reaction zone to the metal fiber solid as the premixture gets richer. This qualitatively matches experimental results reported in Abdelall et al. [2]. Similarly, the energy conversion efficiency ζ and total input power increases with rising equivalence ratio.

3.4.3. *Variation of emissivity of the metal fiber*

The development of maximum gas temperature and the average temperature of the metal fiber outer surface T_{fib} is studied by varying the emissivity of the metal fiber ϵ_{fib} from 0.25 to 0.95 at $P_{th} = 90$ kW ($F_R = 780$ kW/m^2). As illustrated in Fig. 15, the radiation efficiency increases from 9% up to 18% which clearly depends on the mean surface temperature of the metal fiber outlet. Simulations show a strong decrease of

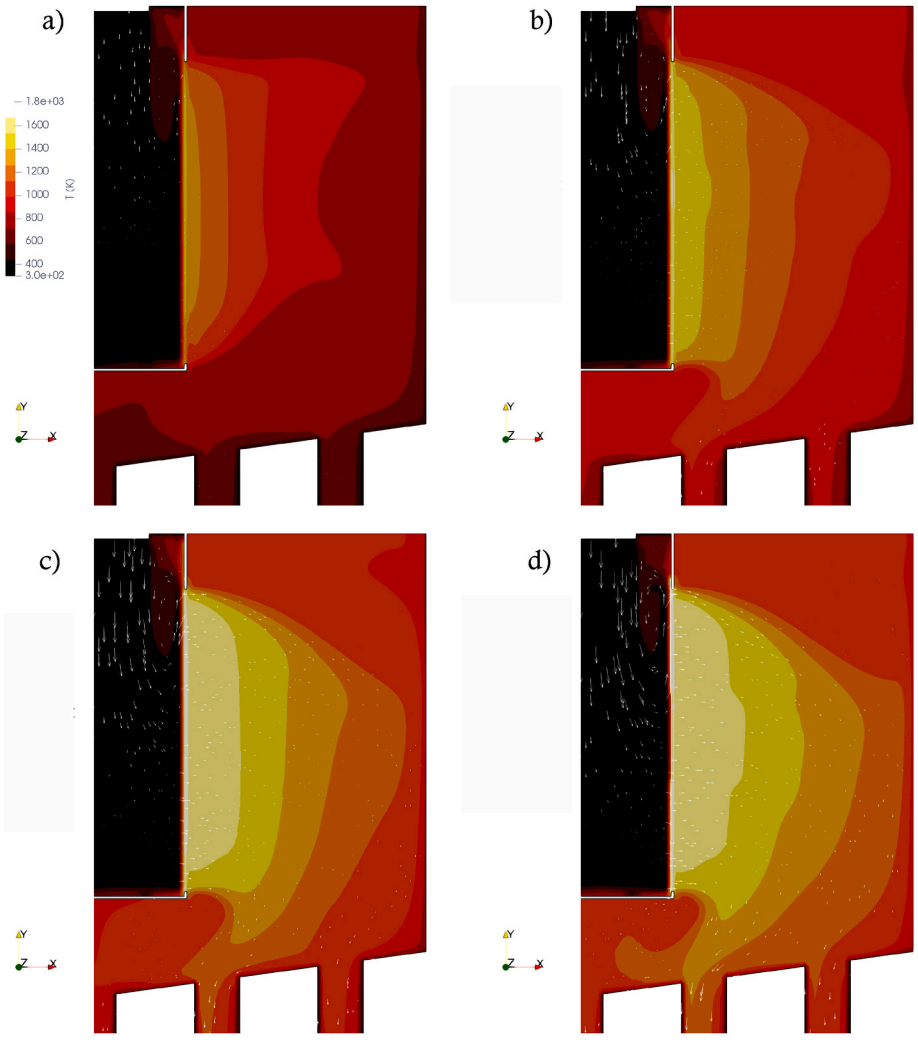


Fig. 12. Contour plot of gas temperature for various operating points: 30 kW (a), 60 kW (b), 90 kW (c), 120 kW (d).

T_{fib} ranging from 1600 K to 1400 K, whereas T_{max} remains in the range between 1750 K and 1700 K.

3.4.4. *Comparative study of combustion chamber designs*

The fully automated tool chain allows a quick comparison of different design variants on the basis of important performance parameters, although only for rotationally symmetrical combustion chamber geometries. In the present comparative study, the height H and the diameter D (see Fig. 3) of the cylindrical burner were varied for three different designs:

- D1: $H = 240$ mm x $D = 220$ mm
- D2: $H = 310$ mm x $D = 110$ mm
- D3: $H = 240$ mm x $D = 150$ mm

The temperature distribution is shown in Fig. 16 for all three designs at $P_{th} = 90$ kW. From the contour plot of design D1, it can be clearly seen that there is a significant recirculation of hot gas in the upper part of the combustion chamber, which subsequently leads to a lower flow rate through the metal fiber in this section. In this design, the diameter ratio between the vertical domain inlet and the radial porous inlet is too large, which enhances the formation of recirculation in the inflow section (also visible in D3). Performance parameters for all three design variants are given in Fig. 17. It can be seen that all parameters are of approximately the same order of magnitude, whereas the radiation efficiency is increased by 2–3% for design D1 due to its larger surface area of the metal fiber layer. However, Design D2 offers a slightly better overall energy conversion rate than the other designs. Compared with D1 and D3, design D2 shows an optimum flow inside the burner cylinder, ensuring straight and uniform inflow of the porous region. Thus, a significantly lower temperature, peaking at 1570 K, and a correspondingly lower NO_x generation is observed for D2 in Fig. 17. Compared to the NO concentration 5.6 ppm at the outlet of D3, a slight increase of the NO concentration up to 6.7 ppm is observed for D1.

4. Conclusions

We presented a newly developed numerical framework for modelling surface-stabilized laminar combustion in a gas-fired condensing boiler which is subsequently employed to study NO_x formation and thermal parameters in various geometric and parametric configurations.

The predictive capability of the numerical framework was validated by comparing calculated flame response and emission characteristics to experimental and simulated data from literature as well as data from

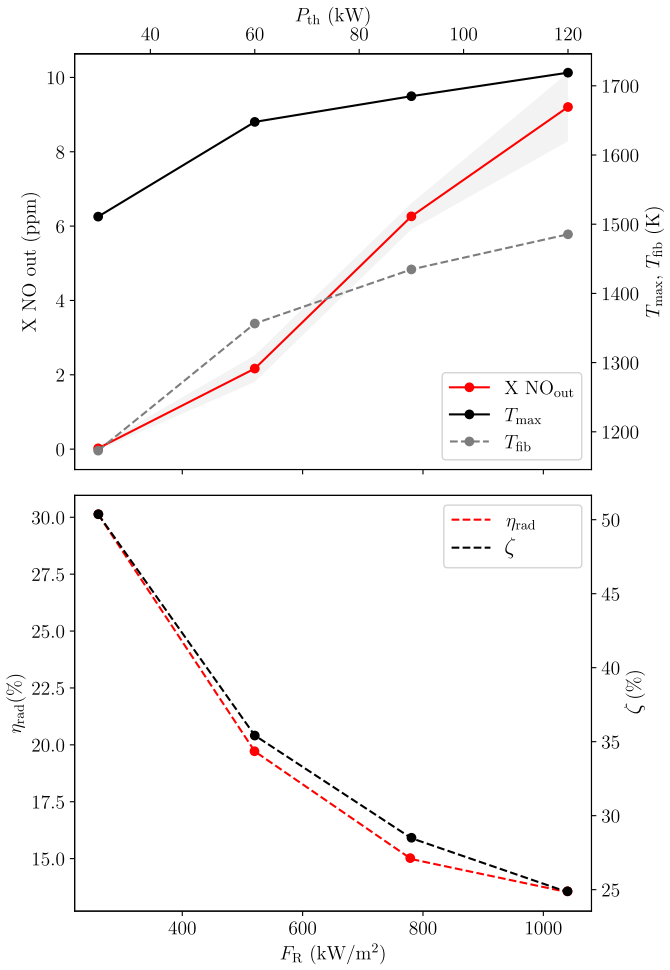


Fig. 13. Combustion characteristics at different operating points P_{th} or firing rates F_R: mean NO concentration at outlet, maximum gas temperature and average surface temperature of the fiber metal layer (top), decreasing radiation efficiency of the burner η_{rad} and the energy conversion efficiency ζ with increasing firing rate (bottom).

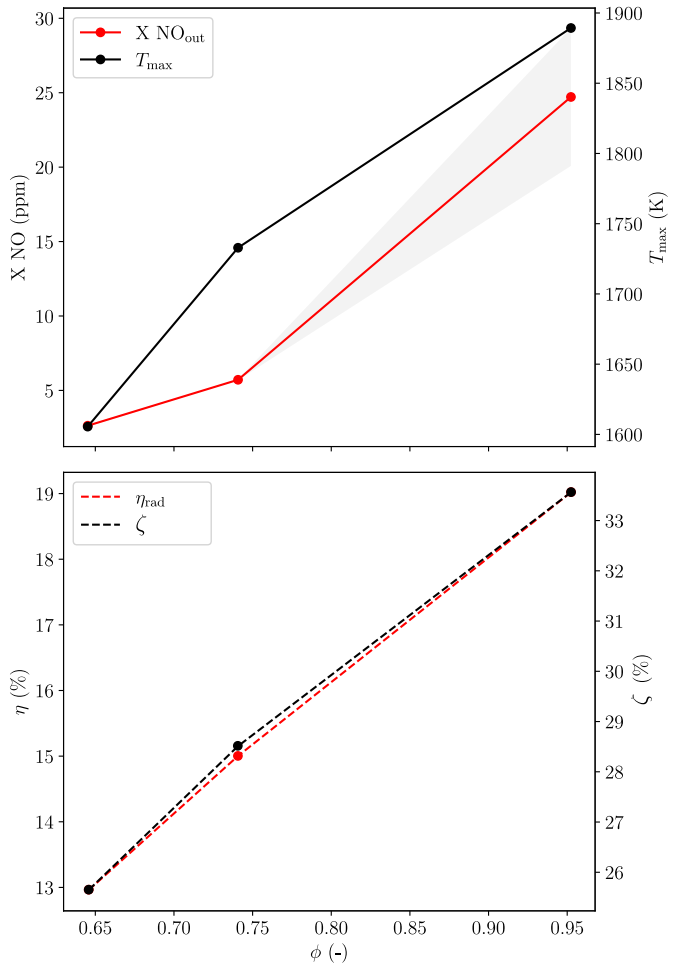


Fig. 14. Performance quantities plotted as a function of equivalence ratio ϕ at P_{th} = 90 kW (resp. F_R = 780 kW/m^2): Development of peak temperature in radial direction (sample line C) and mean NO concentration at the domain outlet including the variability band (top) and radiation efficiency η_{rad} and the energy conversion efficiency ζ (bottom).

own measurements at a full-scale condensing boiler (see sec. 3.3). These tests showed a reasonable agreement of the combustion characteristics between simulations and experimental data in a broad range of scenarios, despite model simplifications e.g., unity Lewis number of diffusion processes and steady-state combustion.

By deliberately neglecting specific solver components (see sec. 3.2) we established that the model accuracy with respect to flame position and temperatures requires the consideration of all relevant thermal and dynamical interaction mechanisms between the porous solids and the gas flow: effective thermal diffusion due to dispersive flow in porous media, heat exchange between porous solid and fluid phase and Darcian flow resistance. We identified the volumetric heat transfer and the effective thermal conductivity of the fluid due to thermal interactions with porous solids as key components in establishing a stable and uniform flame front and thus correctly predicting flame temperature and NO concentration. It appears reasonable that a missing heat exchange channel between fluid and porous structure could lead to delayed ignition and given a thin, porous layer could make the difference between combustion inside or outside of that layer.

At the operating point used for model validation (see sec. 3.3), the simulated NO_x concentration underestimates the measurement by

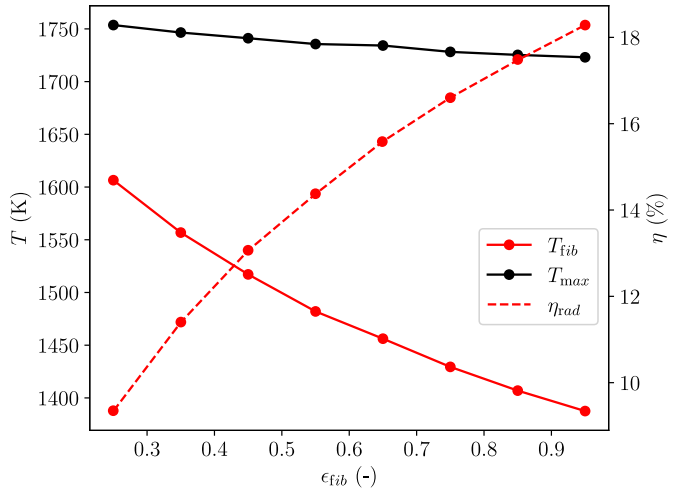


Fig. 15. Mean surface temperature of the metal fiber T_{fib} along sample line B (vertical) and radiation efficiency η_{rad} for P_{th} = 90 kW (resp. F_R = 780 kW/m^2) as a function of fiber emissivity ϵ_{fib}.

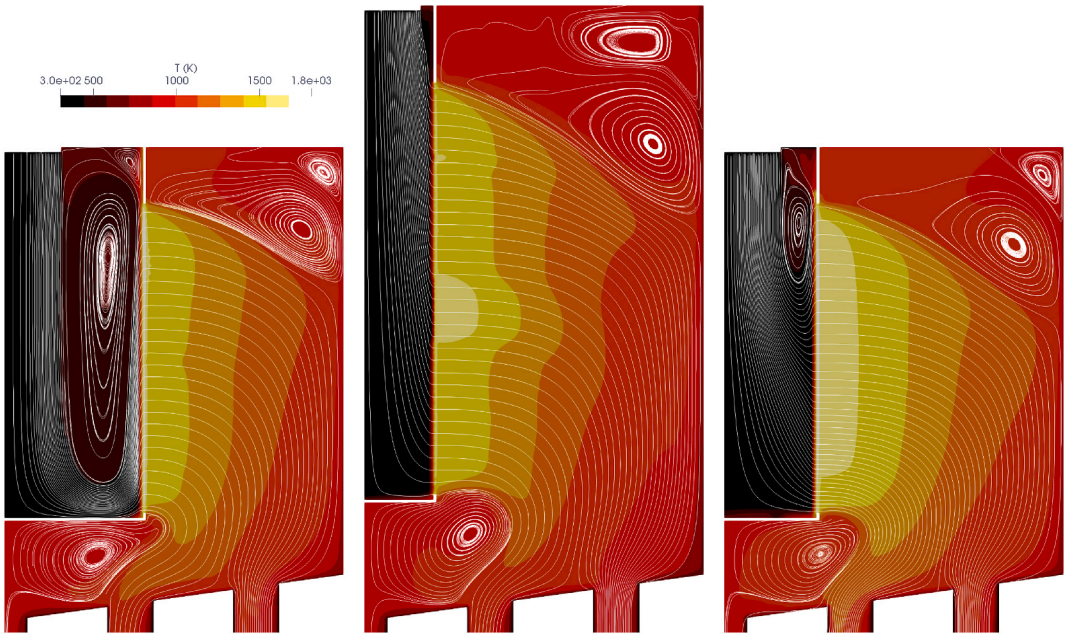


Fig. 16. Temperature distribution and streamlines for three different designs at $P_{th} = 90$ kW: D1 (left), D2 (middle), D3 (right).

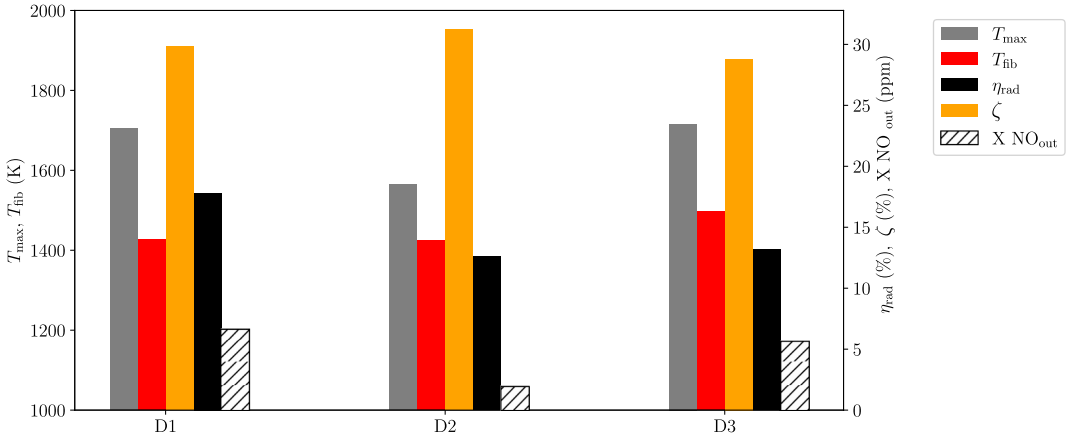


Fig. 17. Performance parameters for designs D1, D2 and D3.

approximately 25% on average, while predicting other species concentrations with higher accuracy. Since NO_x formation is particularly sensitive to flame temperature, the observed strong variation of the maximum temperature along the cylinder height due to non-uniform inflow conditions is a likely cause for this deviation. As shown in sec. 3.4.4 more uniform inflow conditions based on geometrical adaptations of the inner cylinder could alleviate this problem and allow for overall lower flame temperature and NO_x concentration while preserving energy output.

Studying the change of system performance parameters like flame temperature, NO concentration and energy conversion efficiency with varying input parameters like equivalence ratio or firing rate (see sec. 3.4.1 and 3.4.2) we identified dependencies between these quantities. The observed trends e.g., a near-linear rise in NO concentration with firing rate, provide indications on how to adjust the combustion process towards preferred operation conditions. When attaining higher firing rates and richer mixes, the combustion chemistry shows an increasingly oscillatory behavior of the NO formation. Hence the predictive accuracy for NO concentration in the combustion chamber for these regimes must be considered limited and further efforts towards adjusting the chemical reaction model would be required.

The heat transferred to the combustion chamber walls and subsequently delivered to the boiler water is dominated by the radiative heat emitted by the surface of the metal fiber. Compared to reference values from literature, simulations show a qualitative agreement of the estimated radiation efficiency of the surface-stabilized burner for various operation conditions. Capturing the radiative energy interchange between cooled surfaces of arbitrary geometries and the hot metal fiber by a more advanced radiation model would further improve the model accuracy, though likely at the expense of significantly increased computational costs.

Overall, the presented numerical framework delivers accurate results with respect to thermal quantities and approximate NO concentrations for a practical range of operation conditions of a condensing boiler. Due to simplification of the computational domain and the assumption of steady-state flow conditions in the combustion chamber, simulation

results can be obtained without exhausting computational resources. This enables an easy integration of the present numerical framework into an industrial product design process, offering the capacity of deriving indications for the optimization of the parametric und geometric configuration for lean surface stabilized gas combustion processes with respect to NO_x formation and energy efficiency.

Credit author statement

Sandro Erne: Writing & Editing, Software, Methodology, Formal analysis, Validation, Visualization. **Georg Scheger**: Writing & Editing, Data-Acquisition, Formal analysis, Validation. **Wolfgang Wiedemair**: Writing & Editing, Project administration, Funding acquisition, Supervision.

Declaration of competing interest

The authors declare that they have no known competing financial interests or personal relationships that could have appeared to influence the work reported in this paper.

Data availability

The data that has been used is confidential.

Acknowledgments

Financial support by the Swiss Federal Commission for Technology and Innovation - Grant No. 27830.1 PFES-ES - is gratefully acknowledged.

Appendices.

A. *Radiation and conduction correction of temperature measurements*

The protection tube's open end on the hot gas side and the coupling head of the thermocouple are glued and sealed together. Conductive heat losses in the ceramic thermocouple protection tube were neglected. The following heat rate balance is assumed:

$$Q_{\mathrm{rad}} = Q_{\mathrm{conv}} \tag{16}$$

The estimated radiative heat rate between the thermocouple and its adjacent walls reads

$$Q_{\mathrm{rad}} = \epsilon_{\mathrm{pt}}(T_{\mathrm{m}})A_{\mathrm{pt}}\sigma[F_{\mathrm{pt-cyl}}(T_{\mathrm{m}}^4 - T_{\mathrm{cyl}}^4) + (1 - F_{\mathrm{pt-cyl}})(T_{\mathrm{m}}^4 - T_{\mathrm{fib}}^4)] \tag{17}$$

where $\epsilon_{\mathrm{pt}}(T_{\mathrm{m}})$ is the emissivity of the protection tube [40], A_{pt} is the outer surface of the protection tube. The view factor between the cylindrical protection tube and the surface of the metal fiber surface was found analytically, yielding $F_{\mathrm{pt\text{-}cyl}} = 0.71$ for the measurement position closest to the metal fiber surface. An averaged temperature $T_{\mathrm{cyl}} = 400$ K for the combustion chamber wall and an averaged fiber temperature $T_{\mathrm{fib}} = 1450$ K were assumed for estimating the emitted radiation heat of the tube's adjacent walls. The convective heat rate is proposed as follows:

$$Q_{\mathrm{conv}} = A_{\mathrm{pt}}h_{\mathrm{pt}}(T_{\mathrm{m}} - T_{\mathrm{f}}). \tag{18}$$

Herein T_{gas} is the real gas temperature, $h_{\mathrm{pt}} = 2\ \mathrm{Nu}(T_{\mathrm{gas}})k_{\mathrm{pt}}(T_{\mathrm{m}})/D_{\mathrm{out}}$ is the total heat transfer coefficient between hot gas and the protection tube, calculated from the tube's thermal conductivity $k_{\mathrm{pt}}(T_{\mathrm{m}})$ [20] and the outer diameter D_{out}. Nu is calculated for every measurement position, based on the velocity magnitude from the simulation.

To properly estimate the influence of radiation on the measured gas temperature T_{m}, eq. (16) was solved iteratively for T_{f}. Fig. 18 shows the gas temperature profile (sample line A) from experiments, which have been corrected for radiation losses.

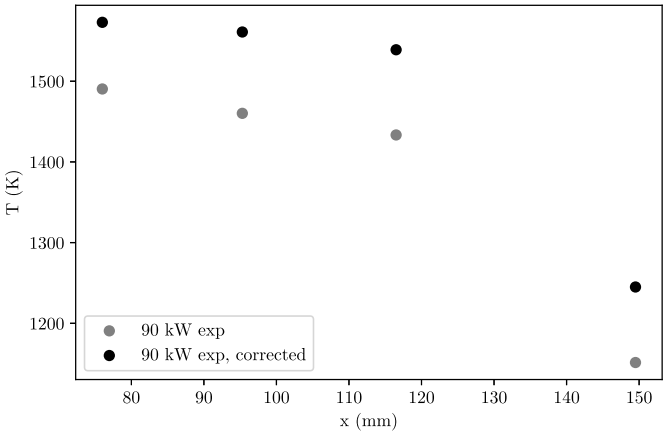


Fig. 18. Measured temperature T_{m} along sample line A and radiation corrected values for operating point $P_{\mathrm{th}} = 90$ kW.

B. Verification of numerical methods

The developed numerical framework was extensively tested by comparing its predictions to experimental as well as numerical results from literature. It is noteworthy that, compared to the lean premixed combustion in the condensing boiler under investigation, the following laminar combustion systems mostly operate at fuel-rich conditions.

All computational grids were generated using the utility `blockMesh` from OpenFOAM® which creates a purely hexahedral mesh.

Conjugate heat transfer

To assess the validity of the implemented conjugate heat transfer capabilities in the present code, the stationary flow over a conductive slab with conjugate forced convection heat transfer following Vynnycky et al. [43] was investigated. Laminar flow conditions and a constant fluid temperature T_∞ were prescribed at the fluid domain inlet. At the solid heated side, a constant temperature T_C was imposed. Thermal conduction in the slab and convection in the fluid are characterized by the thermal conductivity ratio of the solid region and the fluid region $k = 5$. As shown in Fig. 19, the predicted non-dimensional temperature along the fluid-solid interface $T_L = (T_f - T_\infty)/(T_C - T_\infty)$ is in a reasonable agreement with the analytical solution.

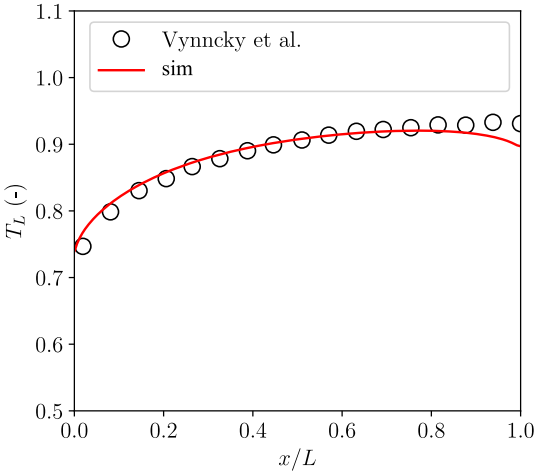


Fig. 19. Conjugate boundary temperature T_L at Re = 500, Pr = 0.01.

Kinetic mechanism for methane-air flames

The propagation of a laminar, quasi one-dimensional flame front was simulated using the elaborate GRI-3.0 combustion mechanism and compared to experimental data. The adiabatic burning velocity s_L, the adiabatic flame temperature T_a and the NO formation in methane/air flames by means of the molar fraction of nitrogen oxide are evaluated. A constant mass flow of the reactants was defined at the inlet and von-Neumann boundary conditions were defined at the outlet, assuming ambient pressure. The comparison between the numerical results and experimental studies [5,42] is shown in.Fig. 20 At low equivalence ratios ($\phi = 0.7 - 0.8$) a reasonable agreement between the calculated laminar burning velocity and experiments is observed. Towards higher equivalence ratios the measured velocities are underpredicted due to limited ODE solver capabilities in OF-5.x, as stated in Yang et al. [48]. Dasgupta et al. [12] also observed a significant under prediction of the laminar burning velocity for the lean region $\phi > 0.7$, using unity Lewis number for all species.

The simulated adiabatic flame temperature T_a as a function of fuel equivalence ratio ϕ of the condensing boiler is plotted and compared to Law [27] in Fig. 21-right. The plot shows that in the expected operating range a good match of the calculated adiabatic temperature with the numerical results is obtained.

The NO concentration as a function of equivalence ratio for the used chemical mechanism is assessed and compared to experimentally sampled probes of the burnt gases from Coppens et al. [11]. Looking at Fig. 21-left, it can be seen that on the lean-side the molar fraction of NO is overestimated with increasing fuel equivalence ratio. In Park [11], a similar behavior was found from simulations of NO_x formation in methane/air lean premixed combustion systems using the detailed kinetic mechanism GRI 3.0.

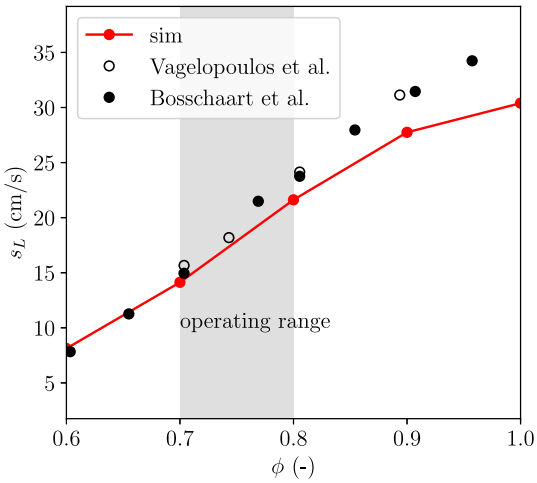


Fig. 20. Laminar flame velocity over equivalence ratio at a pressure of 1 atm.

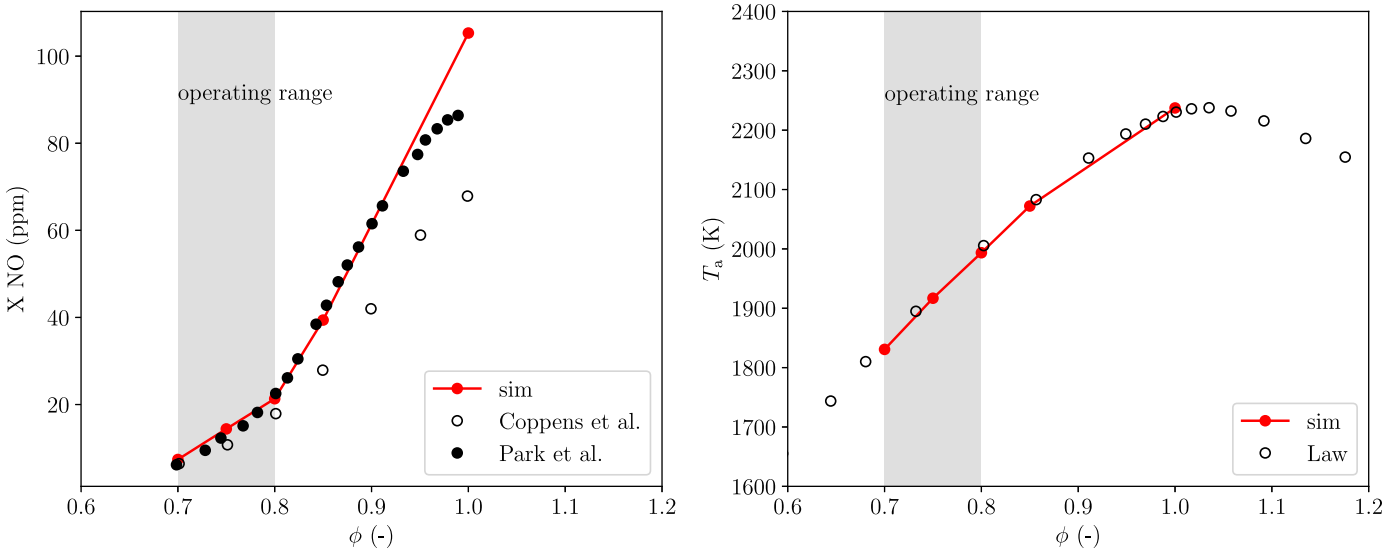


Fig. 21. Molar fraction of NO (left) and adiabatic combustion temperature (right) over equivalence ratio.

Laminar partially-premixed flame

Temperature distribution and emission characteristics of laminar partially-premixed combustion were compared to experimental data from Bennett et al. [4], where measurements were carried out on an axi-symmetric flame configuration with a primary methane-air flow and an oxidizer co-flow. An equivalence ratio of $\phi = 2.464$ was prescribed at the primary inflow to compare the predicted temperature and species concentrations against measurement data. Adiabatic walls and gaseous radiation were assumed in the numerical model.

As can be seen from Fig. 22, the axial position of the peak temperature (flame height H_t) agrees well with the experimental data. Compared to the experimental profiles of the species, the molar fraction of OH is well predicted by the numerical model whereas the prediction of CO_2 is inaccurate but nevertheless shows a reasonable agreement. The molar fraction of H_2O is overestimated by approximately 25%.

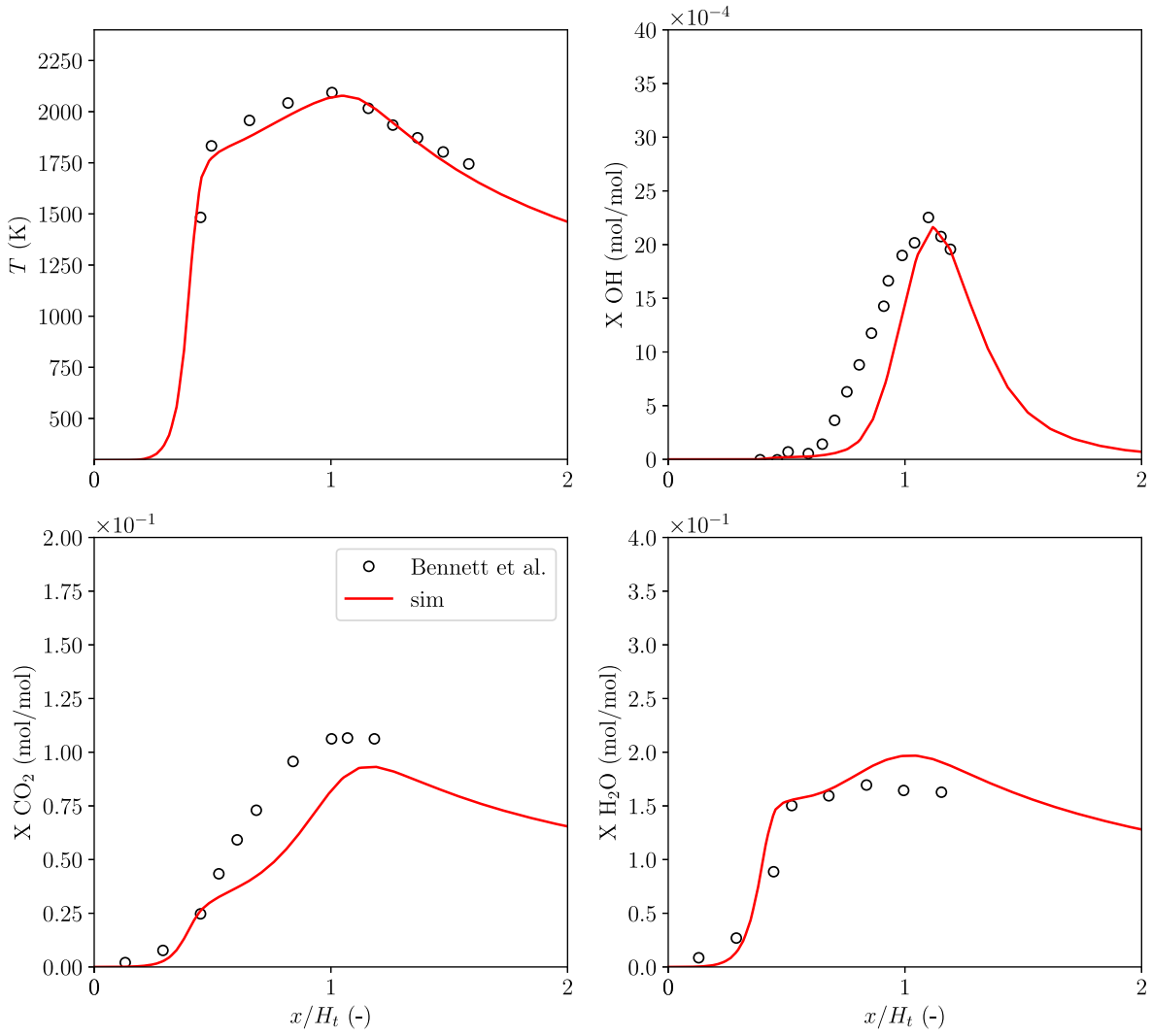


Fig. 22. Comparison of simulated and experimental results along flame centerline for laminar combustion: Temperature (top-left), molar fraction of OH (top-right), molar fraction of CO_2 (bottom-left) and molar fraction of H_2O (bottom-right).

Prediction of NO

The experimental and numerical study of an unconfined laminar flame in a co-flowing oxidizer jet from Smooke et al. [37] was used to validate the prediction of NO_x formation in laminar combustion using the kinetic mechanism GRI 3.0. Constant mass flows were imposed at the premixed methane-air inlet and the surrounding co-oxidizer jet. More details about the experimental configuration can be found in Ref. [37]. In Fig. 23, the computed and experimental NO mole fractions along the domain centerline are compared. The maximum peak position of the NO concentration from experiments is well captured by the GRI 3.0 mechanism. The calculated molar fraction from GRI 3.0 slightly overpredicts the maximum peak from experiments and drops slightly faster with distance from the inlet.

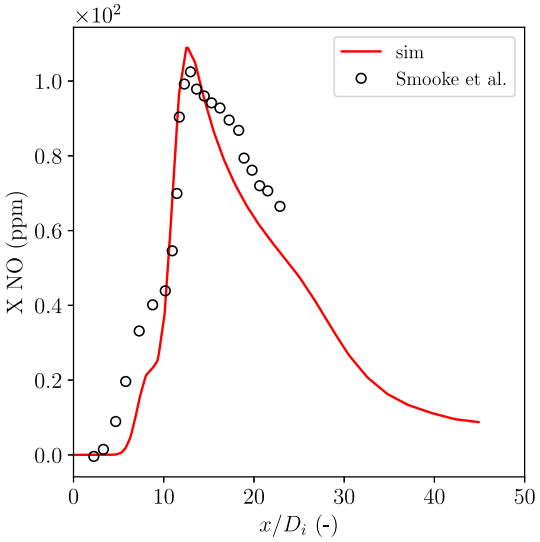


Fig. 23. NO_x modeling validation: molar fraction of NO along centerline.

C. *Effective thermal conductivity*

In the porous zone an effective thermal conductivity $k_{f,e_{ij}}$ of the gas phase is introduced, as proposed in Yang and Nakayama [47]. The effective thermal conductivity tensor reads

$$k_{f,e_{ij}} = k_{f,stag_{ij}} + \varepsilon k_{f,disp_{ij}} \tag{19}$$

where $k_{f,stag_{ij}}$ is the stagnant thermal conductivity tensor and $k_{f,disp_{ij}}$ is the thermal dispersion tensor due to dispersive behavior of the porous flow. To compute $k_{f,stag_{ij}}$ and $k_{f,disp_{ij}}$ we approximate the cylindrical pores by squared ones, in order to use a slight modification of the computations from Ref. [47], sec. 3, and obtain

$$k_{stag_{rr}} = \frac{\varepsilon k_f + (1-\varepsilon)k_s}{1 + \frac{(k_f - k_s)^2}{k_f k_s} \frac{\frac{1}{R_{a_x}}\left(1-\frac{D_x}{H_x}\right)\frac{D_x}{H_x} + \frac{1}{R_{b_x}}\left(1-\frac{C_{yx}}{H_x}\right)\frac{C_{yx}}{H_x} + \frac{1}{R_{c_x}}\left(1-\frac{C_{zx}}{H_x}\right)\frac{C_{zx}}{H_x}}{\frac{1}{R_{a_x}} + \frac{1}{R_{s_x}} + \frac{1}{R_{b_x}} + \frac{1}{R_{c_x}} + \frac{1}{R_{f_x}}}} \tag{20}$$

$$k_{stag_{\phi\phi}} = \frac{\varepsilon k_f + (1-\varepsilon)k_s}{1 + \frac{(k_f - k_s)^2}{k_f k_s} \frac{\frac{1}{R_{a_y}}\left(1-\frac{D_y}{H_y}\right)\frac{D_y}{H_y} + \frac{1}{R_{b_y}}\left(1-\frac{C_{zy}}{H_y}\right)\frac{C_{zy}}{H_y} + \frac{1}{R_{c_y}}\left(1-\frac{C_{xy}}{H_y}\right)\frac{C_{xy}}{H_y}}{\frac{1}{R_{a_y}} + \frac{1}{R_{s_y}} + \frac{1}{R_{b_y}} + \frac{1}{R_{c_y}} + \frac{1}{R_{f_y}}}} \tag{21}$$

$$k_{stag_{zz}} = k_{stag_{\phi\phi}} \tag{22}$$

where the heat resistances are given by

$$R_{a_x} = \left(\frac{H_x - D_x}{k_f} + \frac{D_x}{k_s}\right)\frac{1}{D_y D_z} \tag{23}$$

$$R_{s_x} = \infty \tag{24}$$

$$R_{b_x} = \left(\frac{H_x - C_{yx}}{k_f} + \frac{C_{yx}}{k_s}\right)\frac{1}{C_{yz}(H_y - D_y)} \tag{25}$$

$$R_{c_x} = \left(\frac{H_x - C_{zx}}{k_f} + \frac{C_{zx}}{k_s}\right)\frac{1}{C_{zy}(H_z - D_z)} \tag{26}$$

$$R_{f_x} = \frac{H_x}{(k_f(H_y H_z - D_y D_z - C_{yz}(H_y - D_y) - C_{zy}(H_z - D_z)))} \tag{27}$$

$$R_{a_y} = \left(\frac{H_y - D_y}{k_f} + \frac{D_y}{k_s}\right)\frac{1}{H_z D_x - C_{yx}C_{yz}} \tag{28}$$

$$R_{s_y} = \frac{H_y}{k_s C_{yx} C_{yz}} \tag{29}$$

$$R_{b_y} = \infty \tag{30}$$

$$R_{c_y} = \infty \tag{31}$$

$$R_{f_y} = \frac{H_y}{k_f (H_z H_x - H_z D_x)} \tag{32}$$

and the dimension definitions can be found in [47, Figs. 1 and 2]. The thermal dispersion is the same as in [47, Sec. 5], i.e. for the laminar regime

$$k_{\mathrm{disp}_{rr}} = 0.15\, k_f \frac{\mathrm{Pe}^2}{2 + 1.1 \frac{\mathrm{Pe}^{0.6}}{\mathrm{Pr}^{0.27}}} \tag{33}$$

$$k_{\mathrm{disp}_{\phi\phi}} = \frac{0.15}{20}\, k_f \frac{\mathrm{Pe}^2}{2 + 1.1 \frac{\mathrm{Pe}^{0.6}}{\mathrm{Pr}^{0.27}}} \tag{34}$$

$$k_{\mathrm{disp}_{zz}} = k_{\mathrm{disp}_{\phi\phi}} \tag{35}$$

where the Péclet number Pe is based on the Darcian flow velocity and the characteristic diameter. According to the coordinate system shown in Fig. 4, $rr = xx$ and $zz = yy$.

References

[1] UC San Diego, Chemical-Kinetic Mechanisms for Combustion Applications, Mech. Aerosp. Eng. (Combust. Res.). http://combustion.ucsd.edu, 2016.

[2] M.M. Abdelaal, M.K. El-Riedy, A.M. El-Nahas, Effect of oxygen enriched air on porous radiant burner performance and NO emissions, Exp. Therm. Fluid Sci. 45 (feb 2013) 163–168, https://doi.org/10.1016/j.expthermflusci.2012.10.021.

[3] Amanda J. Barra, Janet L. Ellzey, Heat recirculation and heat transfer in porous burners, Combust. Flame 137 (1–2) (apr 2004) 230–241, https://doi.org/10.1016/j.combustflame.2004.02.007.

[4] Beth Anne V. Bennett, Charles S. McEnally, Lisa D. Pfefferle, D Smooke Mitchell, Computational and experimental study of axisymmetric coflow partially premixed methane/air flames, Combust. Flame 123 (4) (dec 2000) 522–546, https://doi.org/10.1016/s0010-2180(00)00158-9.

[5] K. Bosschaart, Detailed analysis of the heat flux method for measuring burning velocities, Combust. Flame 132 (1–2) (jan 2003) 170–180, https://doi.org/10.1016/s0010-2180(02)00433-9.

[6] S.S. Brown, Variability in nocturnal nitrogen oxide processing and its role in regional air quality, Science 311 (5757) (jan 2006) 67–70, https://doi.org/10.1126/science.1120120.

[7] EDF CEA, Opencascade. Salome: the Open Source Integration Platform for Numerical Simulation, 2010.

[8] Carlo Cintolesi, Håkan Nilsson, Andrea Petronio, Vincenzo Armenio, Numerical simulation of conjugate heat transfer and surface radiative heat transfer using the p1 thermal radiation model: parametric study in benchmark cases, Int. J. Heat Mass Tran. 107 (apr 2017) 956–971, https://doi.org/10.1016/j.ijheatmasstransfer.2016.11.006.

[9] A. Colorado, V. McDonell, Surface stabilized combustion technology: an experimental evaluation of the extent of its fuel-flexibility and pollutant emissions using low and high calorific value fuels, Appl. Therm. Eng. 136 (may 2018) 206–218, https://doi.org/10.1016/j.applthermaleng.2018.02.081.

[10] Andres Colorado, Dimas Avila, Vincent Mcdonell, An Experimental Study of the Stability Limits and Emissions of a Surface-Stabilized Combustion Burner Using Biogas and Natural Gas, 9th U. S. National Combustion Meeting, 05 2015.

[11] F.H.V. Coppens, J. De Ruyck, A.A. Konnov, Effects of hydrogen enrichment on adiabatic burning velocity and NO formation in methane/air flames, Exp. Therm. Fluid Sci. 31 (5) (apr 2007) 437–444, https://doi.org/10.1016/j.expthermflusci.2006.04.012.

[12] Adhiraj Dasgupta, Esteban Gonzalez-Juez, Daniel C. Haworth, Flame simulations with an open-source code, Comput. Phys. Commun. 237 (apr 2019) 219–229, https://doi.org/10.1016/j.cpc.2018.11.011.

[13] Camilo Echeverri-Uribe, Andrés A. Amell, Experimental evaluation of the surface-stabilized combustion of a confined porous inert media burner, Combust. Sci. Technol. 192 (2) (feb 2019) 335–358, https://doi.org/10.1080/00102202.2019.1565493.

[14] Fawzy El-Mahallawy, SE-Din Habik, Fundamentals and Technology of Combustion, Elsevier, 2002.

[15] Kevin G. Field, Mary A. Snead, Yukinori Yamamoto, Kurt A. Terrani, Handbook on the Material Properties of Fecral Alloys for Nuclear Power Production Applications (Fy18 Version: Revision 1), Oak Ridge National Lab.(ORNL), Oak Ridge, TN (United States), 2018. Technical report.

[16] M. Frenklach, Hai Wang, M. Goldenberg, Gregory Smith, D. Golden, C. Bowman, R. Hanson, W. Gardiner, Vitali Lissianski, Gri-mech—an Optimized Detailed Chemical Reaction Mechanism for Methane Combustion, 2000, 01.

[17] Fursenko Roman, Anatoly Maznoy, Egor Odintsov, Kirdyashkin Alexander, Sergey Minaev, Sudarshan Kumar, Temperature and radiative characteristics of cylindrical porous ni–al burners, Int. J. Heat Mass Tran. 98 (jul 2016) 277–284, https://doi.org/10.1016/j.ijheatmasstransfer.2016.03.048.

[18] B. Garten, F. Hunger, D. Messig, B. Stelzner, D. Trimis, C. Hasse, Detailed radiation modeling of a partial-oxidation flame, Int. J. Therm. Sci. 87 (68–84) (jan 2015), https://doi.org/10.1016/j.ijthermalsci.2014.07.022.

[19] Michael Golombok, C. Leslie, Shirvill. Emissivity of layered fibrous materials, Appl. Opt. 27 (18) (sep 1988) 3921, https://doi.org/10.1364/ao.27.003921.

[20] G.V.C. VDI, Verein deutscher ingenieure vdi-gesellschaft verfahrenstechnik und chemieingenieurwesen (gvc), vdi-wärmeatlas. 10 (2006) 2006.

[21] Jörn Hinrichs, Daniel Felsmann, Stefan Schweitzer-De Bortoli, Heinz-Jörg Tomczak, Heinz Pitsch, Numerical and experimental investigation of pollutant formation and emissions in a full-scale cylindrical heating unit of a condensing gas boiler, Appl. Energy 229 (nov 2018) 977–989, https://doi.org/10.1016/j.apenergy.2018.08.011.

[22] IEA, Coal-fired Power, IEA, Paris, 2021. Technical report, https://www.iea.org/reports/coal-fired-power.

[23] IEA, Natural Gas-Fired Power, IEA, Paris, 2021. Technical report, https://www.iea.org/reports/natural-gas-fired-power.

[24] A. Alexander, Konnov. Yet another kinetic mechanism for hydrogen combustion, Combust. Flame 203 (may 2019) 14–22, https://doi.org/10.1016/j.combustflame.2019.01.032.

[25] Krajinska Anna, Magic Green Fuels: Why Synthetic Fuels in Cars Will Not Solve Europe's Pollution Problems, Transport & Environment, 2021. Technical report, https://www.transportenvironment.org/wp-content/uploads/2021/11/2021_12_TE_e-fuels_cars_pollution.pdf.

[26] F.A. Lammers, L.P. H de Goey, The influence of gas radiation on the temperature decrease above a burner with a flat porous inert surface, Combust. Flame 136 (4) (mar 2004) 533–547, https://doi.org/10.1016/j.combustflame.2003.12.010.

[27] K. Chung, Law. *Combustion Physics*, Cambridge University Press, 2006, https://doi.org/10.1017/cbo9780511754517.

[28] S. A Leonardi, R. Viskanta, J. P Gore, Radiation and thermal performance measurements of a metal fiber burner, J. Quant. Spectrosc. Radiat. Transf. 73 (2–5) (apr 2002) 491–501, https://doi.org/10.1016/s0022-4073(01)00201-1.

[29] Anatoly Maznoy, Kirdyashkin Alexander, Sergey Minaev, Alexey Markov, Nikita Pichugin, Evgeny Yakovlev, A study on the effects of porous structure on the environmental and radiative characteristics of cylindrical ni-al burners, Energy 160 (oct 2018) 399–409, https://doi.org/10.1016/j.energy.2018.07.017.

[30] F. Michael, Modest. *Radiative Heat Transfer*, Elsevier LTD, Oxford, 2013, ISBN 0123869447. URL, https://www.ebook.de/de/product/19724908/michael_f_modest_radiative_heat_transfer.html.

[31] Mahdi Najarnikoo, Mohammad Zabetian Targhi, Hadi Pasdarshahri, Experimental study on the flame stability and color characterization of cylindrical premixed perforated burner of condensing boiler by image processing method, Energy 189 (dec 2019), 116130, https://doi.org/10.1016/j.energy.2019.116130.

[32] Thierry J. Poinsot, Denis P. Veynante, Combustion, Encycl. Computation. Mechan. (2018) 1–30. Second Edition.

[33] J.Y. Ren, F.N. Egolfopoulos, T.T. Tsotsis, NO x emission control of lean methane-air combustion with addition of methane reforming products, Combust. Sci. Technol. 174 (4) (apr 2002) 181–205, https://doi.org/10.1080/713713016.

[34] Nicolás Ripoll, Mario Toledo, Hydrogen and syngas production from methane-acetylene rich combustion in inert porous media burner, Res. Eng. 12 (2021) 100287, https://doi.org/10.1016/j.rineng.2021.100287. ISSN 2590-1230.
[35] Patrick J. Roache, Kirti N. Ghia, Frank M. White, Editorial Policy Statement on the Control of Numerical Accuracy, 1986.
[36] Fabio Schiro, Stoppato Anna, Experimental investigation of emissions and flame stability for steel and metal fiber cylindrical premixed burners, Combust. Sci. Technol. 191 (3) (aug 2018) 453–471, https://doi.org/10.1080/00102202.2018.1500556.
[37] M.D. Smooke, A. Ern, M.A. Tanoff, B.A. Valdati, R.K. Mohammed, D.F. Marran, M. B. Long, Computational and experimental study of no in an axisymmetric laminar diffusion flame, Symposium (International) on Combustion 26 (2) (1996) 2161–2170, https://doi.org/10.1016/s0082-0784(96)80042-7.
[38] Sadaf Sobhani, Bret Haley, Dave Bartz, Jared Dunnmon, John Sullivan, Matthias Ihme, Investigation of lean combustion stability, pressure drop, and material durability in porous media burners, in: Volume 5C: Heat Transfer, American Society of Mechanical Engineers, jun 2017, https://doi.org/10.1115/gt2017-63204.
[39] Catharine Tierney, Susie Wood, Andrew T. Harris, David F. Fletcher, Computational fluid dynamics modelling of ultra-lean porous burners, Prog. Computation. Fluid Dynamics, Int. J. 10 (5/6) (2010) 352, https://doi.org/10.1504/pcfd.2010.035369.
[40] Y.S. Touloukian, D.P. DeWitt, Thermophysical Properties of Matter-The Tprc Data Series. Volume 8. Thermal Radiative Properties-Nonmetallic Solids, Thermophysical and Electronic Properties Information Analysis Center, 1972. Technical report.
[41] Falko Ueckerdt, Christian Bauer, Alois Dirnaichner, Everall Jordan, Romain Sacchi, Gunnar Luderer, Potential and risks of hydrogen-based e-fuels in climate change mitigation, Nat. Clim. Change 11 (5) (may 2021) 384–393, https://doi.org/10.1038/s41558-021-01032-7.
[42] Christine M. Vagelopoulos, Fokion N. Egolfopoulos, Direct experimental determination of laminar flame speeds, Symposium (international) on combustion 27 (1998) 513–519. Elsevier.
[43] M. Vynnycky, S. Kimura, K. Kanev, I. Pop, Forced convection heat transfer from a flat plate: the conjugate problem, Int. J. Heat Mass Tran. 41 (1) (jan 1998) 45–59, https://doi.org/10.1016/s0017-9310(97)00113-0.
[44] Hongmin Wang, Chunzhi Wei, Pinghui Zhao, Taohong Ye, Experimental study on temperature variation in a porous inert media burner for premixed methane air combustion, Energy 72 (aug 2014) 195–200, https://doi.org/10.1016/j.energy.2014.05.024.
[45] Hui Wang, Liejin Guo, Volumetric convective heat transfer coefficient model for metal foams, Heat Tran. Eng. 40 (5–6) (feb 2018) 464–475, https://doi.org/10.1080/01457632.2018.1432045.
[46] Henry G. Weller, Tabor Gavin, Hrvoje Jasak, Christer Fureby, A tensorial approach to computational continuum mechanics using object-oriented techniques, Comput. Phys. 12 (6) (1998) 620–631.
[47] C. Yang, A. Nakayama, A synthesis of tortuosity and dispersion in effective thermal conductivity of porous media, Int. J. Heat Mass Tran. 53 (15–16) (jul 2010) 3222–3230, https://doi.org/10.1016/j.ijheatmasstransfer.2010.03.004.
[48] Yang Qi, Peng Zhao, Haiwen Ge, reactingFoam-SCI: an open source CFD platform for reacting flow simulation, Comput. Fluid 190 (aug 2019) 114–127, https://doi.org/10.1016/j.compfluid.2019.06.008.
[49] Marta Yugo, Alba Soler, A look into the role of e-fuels in the transport system in europe (2030–2050), Concawe Rev. 28 (1) (2019).
[50] Hongyu Zeng, Yuqing Wang, Yixiang Shi, Meng Ni, Ningsheng Cai, Syngas production from CO 2/CH 4 rich combustion in a porous media burner: experimental characterization and elementary reaction model, Fuel 199 (jul 2017) 413–419, https://doi.org/10.1016/j.fuel.2017.03.003.

Nomenclature

Dimensionless Numbers

Nu (−): Nusselt number
Pe (−): Péclet number
Pr (−): Prandtl number
Re (−): Reynolds number

Greek Symbols

χ (−): switch between porous region and free flow region
ε (−): porosity, relative error
η (−): radiation efficiency
κ (W m^{-1} K^{-1}): absorption coefficient
μ (kg m^{-1} s^{-1}): dynamic viscosity
ϕ (−): fuel–air equivalence ratio
ρ (kg m^{-3}): density
σ (W m^{-2} K^{-4}): Stefan-Boltzmann constant
ϵ (−): emissivity
ζ (−): energy conversion efficiency

Roman Symbols

A (m^2): surface area
B (−): buoyancy term
c (−): progress variable
c_p (m^2 s^{-2} K^{-1}): specific heat capacity
D (m^{-2}): Darcy coefficient
D (m): diameter
d (m): pore diameter
F (−): view factor
F (kW m^{-2}): firing rate
F (m^{-1}): Forchheimer coefficient
g (m s^{-2}): gravitational acceleration
G (W m^{-2}): incident radiation
h (J kg^{-1}): specific enthalpy
h (m): grid width
h (W m^{-3} K^{-1}, W m^{-2} K^{-1}): heat transfer coefficient
k (W m^{-1} K^{-1}): thermal conductivity
L (m): length
p (N m^{-2}): pressure
P_{th} (W): thermal power
q (W m^{-2}): heat flux
Q (W): total heat flow rate
r (kg m^{-3}): chemical reaction rate
R (m): radius
S (−): Darcy-Forchheimer source term
s_L (m s^{-1}): laminar flame velocity
T (K): temperature
u (m s^{-1}): velocity
W (mol): molar weight
X (mol mol^{-1}): molar fraction of species
x, y, z (m,m,m): spatial directions
Y (kg kg^{-1}): mass fraction of species

Subscripts

a: adiabatic
b: burnt
conv: convection
cyl: cylindrical wall of burning chamber
disp: dispersive
eff: effective
f: fluid
fib: fiber metal surface
fib-cyl: fiber-cylinder
fuel: fuel
gas: gas temperature
L: laminar
m: measured temperature
max: maximum value
out: outlet
pt: protection tube
pt-cyl: protection tube - cylindrical wall of burning chamber
rad: radiation
s: solid
st: stoichiometric
stag: stagnant
u: unburnt
v: volumetric